

MICROCOPY RESOLUTION TEST CHART  
NATIONAL BUREAU OF STANDARDS 1963-A

**AD-A172 512**

(12)

**DNA-TR-85-158**

**AN ENDOCHRONIC PLASTICITY THEORY FOR CONCRETE**

**K. C. Valanis  
H. E. Read  
S-CUBED  
A Division of Maxwell Labs, Inc.  
P. O. Box 1620  
La Jolla, CA 92038-1620**

**20 February 1985**

**Technical Report**

**CONTRACT No. DNA 001-84-C-0127**

**Approved for public release;  
distribution is unlimited.**

SEP 24 1986

THIS WORK WAS SPONSORED BY THE DEFENSE NUCLEAR AGENCY  
UNDER RDT&E RMSS CODE B341084469 Q93QMXSC00005 H2590D.

**DTIC FILE COPY**

**Prepared for  
Director  
DEFENSE NUCLEAR AGENCY  
Washington, DC 20305-1000**

**86 9 23 051**

## DISTRIBUTION LIST UPDATE

This mailer is provided to enable DNA to maintain current distribution lists for reports. We would appreciate your providing the requested information.

- Add the individual listed to your distribution list.
- Delete the cited organization/individual.
- Change of address.

NAME: \_\_\_\_\_

ORGANIZATION: \_\_\_\_\_

**OLD ADDRESS**

**CURRENT ADDRESS**

\_\_\_\_\_  
\_\_\_\_\_  
\_\_\_\_\_

\_\_\_\_\_  
\_\_\_\_\_  
\_\_\_\_\_

TELEPHONE NUMBER: (    ) \_\_\_\_\_

SUBJECT AREA(S) OF INTEREST:

\_\_\_\_\_  
\_\_\_\_\_  
\_\_\_\_\_

\_\_\_\_\_  
\_\_\_\_\_  
\_\_\_\_\_

DNA OR OTHER GOVERNMENT CONTRACT NUMBER: \_\_\_\_\_

CERTIFICATION OF NEED-TO-KNOW BY GOVERNMENT SPONSOR (if other than DNA):

SPONSORING ORGANIZATION: \_\_\_\_\_

CONTRACTING OFFICER OR REPRESENTATIVE: \_\_\_\_\_

SIGNATURE: \_\_\_\_\_

UNCLASSIFIED

SECURITY CLASSIFICATION OF THIS PAGE

AD-A112-512

REPORT DOCUMENTATION PAGE				Form Approved OMB No. 0704-0188 Exp. Date: Jun 30, 1986	
1a REPORT SECURITY CLASSIFICATION UNCLASSIFIED		1b RESTRICTIVE MARKINGS			
2a SECURITY CLASSIFICATION AUTHORITY N/A since Unclassified		3 DISTRIBUTION/AVAILABILITY OF REPORT Approved for public release; distribution is unlimited.			
2b DECLASSIFICATION/DOWNGRADING SCHEDULE N/A since Unclassified					
4 PERFORMING ORGANIZATION REPORT NUMBER(S) SSS-R-85-7172		5 MONITORING ORGANIZATION REPORT NUMBER(S) DNA-TR-85-158			
6a NAME OF PERFORMING ORGANIZATION S-CUBED	6b OFFICE SYMBOL (If applicable)	7a NAME OF MONITORING ORGANIZATION Director Defense Nuclear Agency		7b ADDRESS (City, State, and ZIP Code) Washington, DC 20305-1000	
6c ADDRESS (City, State, and ZIP Code) A Division of Maxwell Labs, Inc. P. O. Box 1620 La Jolla, CA 92038-1620		9 PROCUREMENT INSTRUMENT IDENTIFICATION NUMBER DNA 001-84-C-0127			
8a NAME OF FUNDING, SPONSORING ORGANIZATION	8b OFFICE SYMBOL (If applicable)	10 SOURCE OF FUNDING NUMBERS			
8c ADDRESS (City, State, and ZIP Code)		PROGRAM ELEMENT NO 62715H	PROJECT NO Q93QMXS	TASK NO C	WORK UNIT ACCESSION NO DH251136
11 TITLE (Include Security Classification) AN ENDOCHRONIC PLASTICITY THEORY FOR CONCRETE					
12 PERSONAL AUTHOR(S) Valanis, K. C. and Read, H. E.					
13a TYPE OF REPORT Technical	13b TIME COVERED FROM 831121 TO 841231	14 DATE OF REPORT (Year, Month, Day) 850220	15 PAGE COUNT 114		
16 SUPPLEMENTARY NOTES This work was sponsored by the Defense Nuclear Agency under RDT&E RMSS Code B341084469 Q93QMXSC00005 H2590D.					
17 COSATI CODES		18 SUBJECT TERMS (Continue on reverse if necessary and identify by block number)			
FIELD	GROUP	SUB-GROUP	Concrete		
11	2		Plasticity, <i>with attention models,</i>		
20	11		Stress and Strain, <i>stress in concrete, etc.</i>		
19 ABSTRACT (Continue on reverse if necessary and identify by block number) A fully three-dimensional endochronic plasticity theory for plain concrete is developed to describe its multi-axial behavior over the stress range below that at which significant cracking occurs. The theory is isotropic and exhibits the important features of concrete behavior, including shear-volumetric coupling, effect of hydrostatic pressure on shear response, hardening, hysteretic effects and stress path dependence. The theory is based on the hypothesis that the current state of stress is a linear functional of the entire history of deformation, with the history defined with respect to a time scale, called intrinsic time, which is itself a property of the material at hand. The theory is proof-tested with remarkable success against an extensive set of complex multi-axial plain concrete data recently obtained by others with a true triaxial device. An analytical procedure for reducing the linear hereditary integral expressions for the stresses to a system of coupled linear ordinary differential equations is described, and a numerical approach is given for treating the resulting governing system of equations under either stress- or strain-controlled conditions.					
20 DISTRIBUTION AVAILABILITY OF ABSTRACT <input type="checkbox"/> UNCLASSIFIED UNLIMITED <input checked="" type="checkbox"/> SAME AS RPT <input type="checkbox"/> DTIC USERS		21 ABSTRACT SECURITY CLASSIFICATION UNCLASSIFIED			
22a NAME OF RESPONSIBLE INDIVIDUAL Betty L. Fox		22b TELEPHONE (Include Area Code) (202) 325-7042	22c OFFICE SYMBOL DNA/STTI		

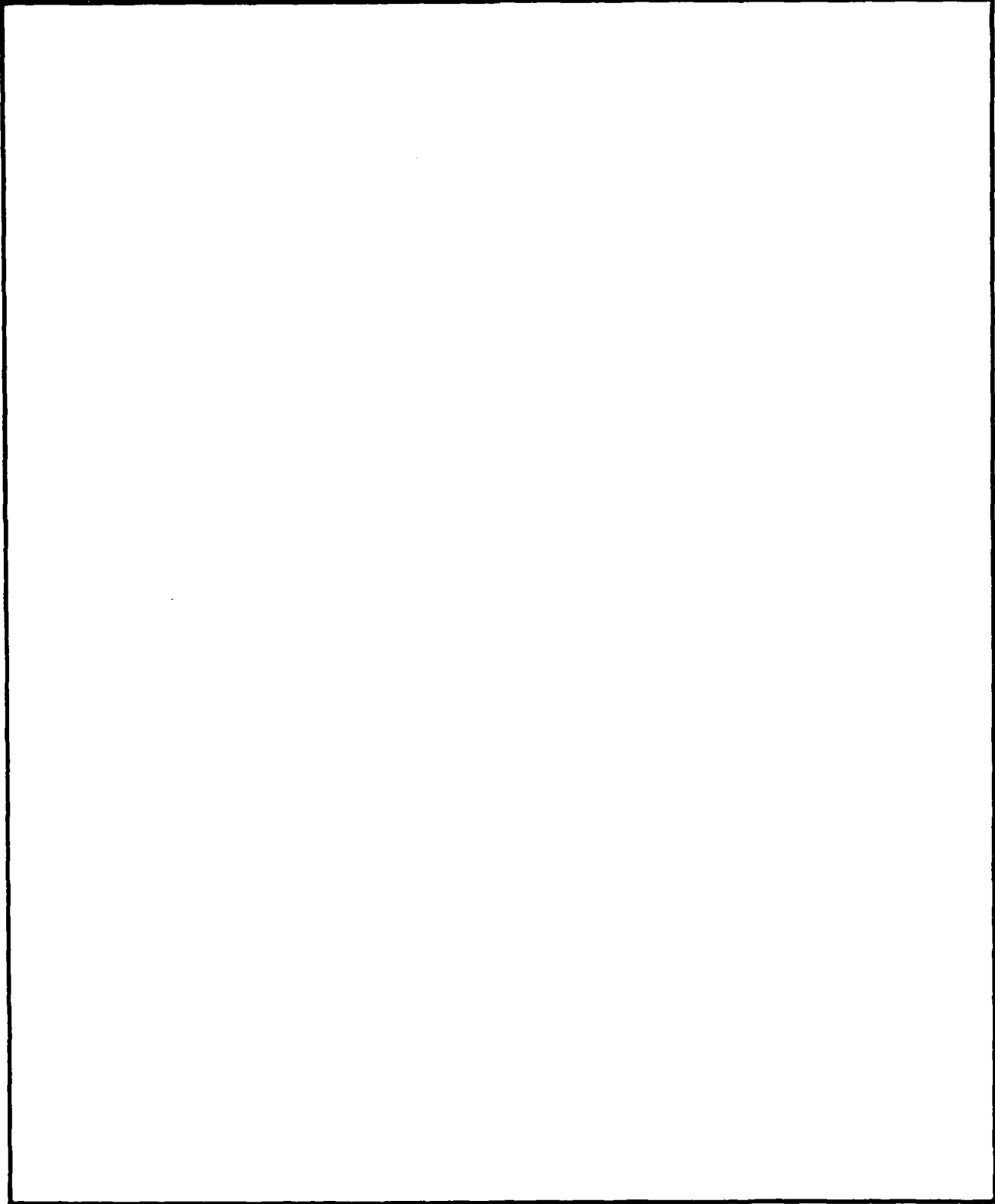
DD FORM 1473, 8/78

33 APR 83 Edition may be used until exhausted  
All other editions are obsolete

SECURITY CLASSIFICATION OF THIS PAGE

UNCLASSIFIED

UNCLASSIFIED  
SECURITY CLASSIFICATION OF THIS PAGE



SECURITY CLASSIFICATION OF THIS PAGE  
UNCLASSIFIED



## TABLE OF CONTENTS

Section	Page
PREFACE .....	iii
LIST OF ILLUSTRATIONS.....	vii
1 INTRODUCTION.....	1
2 THERMODYNAMIC FOUNDATIONS OF THEORY.....	6
2.1 THERMODYNAMIC RELATIONS.....	6
2.2 EVOLUTION EQUATIONS.....	12
2.3 THE NOTION OF INTRINSIC TIME.....	14
2.4 INTEGRAL FORM OF THE EQUATIONS.....	16
2.5 SINGULAR KERNELS.....	20
3 SPECIFIC FORM OF THEORY FOR PLAIN CONCRETE.....	22
3.1 HYDROSTATIC RESPONSE.....	24
3.1.1 The Hardening Function $F_H$ .....	26
3.1.2 Method of Analysis.....	26
3.2 SHEAR RESPONSE.....	29
3.2.1 The Kernel $\rho(z_s)$ .....	30
3.2.2 The Function $F_s$ .....	32
3.2.3 Determination of the Kernel $\rho(w)$ in the Presence of Pressure.....	38
3.2.4 Numerical Procedure for Determining the Kernel Function $\rho(z_s)$ .....	40
4 EVALUATION OF MODEL PARAMETERS FROM PLAIN CONCRETE DATA .....	43
4.1 DETERMINATION OF MODEL PARAMETERS.....	43
4.1.1 Hydrostatic Parameters.....	43
4.1.2 Shear Parameters.....	48
4.2 INTERNAL CONSISTENCY OF MODEL, DATA AND FITTING PROCEDURE.....	57
5 PROOF-TESTS OF MODEL OVER COMPLEX STRESS PATHS....	62
5.1 SERIES NO. 1.....	62
5.2 SERIES NO. 3.....	65
5.3 SERIES NO. 4.....	67
5.4 SERIES NO. 5.....	80
5.5 SERIES NO. 6.....	82

TABLE OF CONTENTS (Concluded)

Section	Page
6 CONCLUSIONS .....	84
7 LIST OF REFERENCES.....	86
APPENDIX A: A PROOF OF EQUATION (3.50).....	89
APPENDIX B: NUMERICAL SCHEME FOR TREATING THE PRESENT CONSTITUTIVE MODEL UNDER STRESS-DRIVEN CONDITIONS .....	93
APPENDIX C: DERIVATION OF EQUATION (4.12).....	97

## LIST OF ILLUSTRATIONS

Figure		Page
1	An elastic system and a plastic system in series..	9
2	Elastic response at unloading and reloading.....	9
3	Typical response of plain concrete to pure hydrostatic compression.....	23
4	Shear response as a function of the hydrostatic compression. ....	23
5	Pressure versus plastic volumetric strain for virgin hydrostatic compression.....	27
6	General form of the relationship between $\sigma_o - \sigma^*$ and $z_H$ .....	27
7	Octahedral normal stress versus octahedral normal strain for virgin hydrostatic compression.....	44
8	Octahedral normal stress versus plastic octahedral normal strain for virgin hydrostatic compression..	44
9	Representation of the $\sigma_o - \sigma^*$ versus $z_H$ relationship by a two-term series of decaying exponentials. The solid circles are the equally-spaced points to which the series was fit.....	47
10	Octahedral normal stress versus octahedral normal strain for pure hydrostatic compression, including unloading and reloading.....	47
11	Octahedral shear stress versus octahedral shear strain for Tests 4-9 to 4-11.....	49
12	Dependence of shear modulus on octahedral shear stress .....	49
13	Dependence of the octahedral shear stress $\tau_o$ on the plastic octahedral shear strain for a fixed hydrostatic pressure of 8 ksi.....	52

LIST OF ILLUSTRATIONS (Continued)

Figure		Page
14	Dependence of the octahedral normal strain $\epsilon_o$ on the octahedral shear stress $\tau_o$ for several different values of constant hydrostatic pressure. Data are from Tests 4-9 to 4-11.....	52
15	Shear-volumetric coupling at a constant hydrostatic pressure of 8 ksi. Data are from Test 4-11 in Reference 17.....	53
16	Dependence of $\gamma_o^D$ on $z_s - z_s^0$ predicted by Eqs. (4.12) and (4.13) for shear at a constant pressure of 8 ksi.....	53
17	Dependence of M on $z_s$ for shear at a fixed hydrostatic pressure of 8 ksi.....	56
18	Measured and predicted responses to a shear at a fixed hydrostatic pressure of 4 ksi (Test 4-9)....	59
19	Measured and predicted responses to shear at a fixed hydrostatic pressure of 6 ksi. (Test 4-10)..	60
20	Measured and predicted responses to shear at a fixed hydrostatic pressure of 8 ksi (Test 4-11)...	61
21	Stress paths for Test 1-1.....	63
22	Predicted and measured response of plain concrete to Test 1-1.....	64
23	Response of plain concrete to circular stress paths in the deviatoric plane.....	66
24	Dependence of pressure $\sigma$ on octahedral strain $\gamma_o$ for Tests 4-1 and 4-2.....	69
25	Measured and predicted responses for Test 4-9.....	71
26	Stress path for Test 4-11.....	72
27	Measured and predicted responses for Test 4-11....	73
28	Measured and predicted responses for Test 4-13....	74
29	Measured and predicted responses for Test 4-15....	75

LIST OF ILLUSTRATIONS (Concluded)

Figure		Page
30	Measured and predicted responses for Test 4-16....	76
31	Major principal stress versus principal strains for Test 4-17.....	77
32	Measured and predicted responses for Test 4-17....	78
33	Measured and predicted responses for Test 4-20....	79
34	Stress paths for Tests 5-1 for 5-3.....	81
35	Measured and predicted responses for Test 6-2.....	83

## SECTION 1

### INTRODUCTION

The ability to predict the behavior and strength of reinforced concrete structures is often crucial for design purposes and depends very strongly on our understanding of, and capability to analytically model, the nonlinear response of plain concrete to applied stresses. From a constitutive modeling viewpoint, plain concrete is an exceedingly complex material whose constitutive properties under general load paths have, to date, largely eluded researchers. As noted by Chen and Suzuki,<sup>(1)</sup> a general constitutive relation capable of describing both pre- and post-failure behavior of plain concrete simply does not exist today. In fact, a general model capable of describing the behavior of plain concrete under all possible conditions, and yet is sufficiently simple for use in design applications, may be out of reach at the present time.

In recent years, a variety of nonlinear constitutive models has been proposed in the literature for describing the response of plain concrete to short-term loads. These models have been based upon nonlinear elasticity,<sup>(2)</sup> classical plasticity,<sup>(3)</sup> hypo-elasticity,<sup>(4)</sup> endochronic plasticity,<sup>(5,6)</sup> bounding surface plasticity,<sup>(7,8)</sup> continuous damage theory,<sup>(9,10)</sup> plastic-fracture theory<sup>(11)</sup> and microstructural considerations.<sup>(12)\*</sup> In almost all cases, the models were developed from, and validated against, data from standard laboratory tests in which at least two of the principal stresses were equal. Some true triaxial experiments have also been performed on concrete, but these have been largely limited to proportional,

---

\*. For a review and critique of various modeling approaches, see Chen and Ting.<sup>(13)</sup>

monotonically-increasing loading to failure.<sup>(14,16)</sup> the results from these tests are inadequate for identifying and characterizing the salient constitutive features of concrete under arbitrary load paths, unloading, stress reversals and reloading, which are generally encountered in practice.

To fill the need for data on the response of plain concrete to complex, multi-axial loading paths, Gerstle, Ko and coworkers recently conducted an extensive laboratory testing program,<sup>(17)</sup> using a true triaxial test device designed specifically for use in studying the multi-axial behavior of geomaterials. This device independently applies three normal stresses of up to 15,000 psi to the sides of 4-inch cubical specimens. The focus of this experimental study was confined to the range of load levels below that at which significant cracking of the plain concrete would occur. A total of 47 different non-standard stress paths were investigated. Of these, a number of paths were chosen to provide insight into possible stress-path dependence.

From the results of this study, it was found that plain concrete exhibits behavior under complex loading which appears to be not well represented by any of the current models. In particular, it was found that the loading surface has the form of a box in principal stress space, with sides parallel to the principal stress axes; hence, the projection of the loading surface on the deviatoric plane is a triangle, which is aligned with the principal deviatoric stress axes in the deviatoric plane so that each of its sides is perpendicular to one of the principal axes. Thus, the loading surface is not affine with the failure surface. Except near the failure surface, the plastic flow law appears to be associated, with the plastic strain rate vector normal to the loading surface at the current stress point. As the failure surface is approached, the plastic strain rate vector

begins to deviate from normality and ultimately becomes normal to the failure surface.

In an effort to analytically represent the results from their experimental study, Stankowski and Gerstle developed a simple, hypo-elastic-type constitutive model<sup>(18)</sup> that is an extension of a previous model by Gerstle.<sup>(19)</sup> The model was applied to several of the complex axisymmetric stress paths studied experimentally and, considering the simplicity of the model, it showed remarkable predictive capability. Several other more complex concrete models<sup>(11,20)</sup> were also exercised around the same paths by Gerstle and Willam,<sup>(33)</sup> but they failed to show comparable predictive capabilities. While the simple model has shown its ability to capture many of the response features of plain concrete under several axisymmetric stress histories, it has not, to date, been extended to, nor validated against, more general loading conditions. In order to capture certain features of behavior that are beyond the scope of the simple theory, and to have a theory that is applicable to general multi-axial loading states, we explored the potential offered by the new endochronic theory for describing the extensive experimental results given in Reference 17.

The new endochronic plasticity theory was originally developed by Valanis,<sup>(21)</sup> and has since been applied with remarkable success to various problems of metal plasticity<sup>(22,23)</sup> and geomaterials.<sup>(24)</sup> The theory is based upon the hypothesis that the current state of stress in a material is a linear functional of the entire history of deformation, with the history defined with respect to a time scale, called intrinsic time, which is itself a property of the material at hand. Such an approach does not require the notion of yield surface nor the specification of unloading-reloading criteria, and these unique features make the theory particularly attractive for describing

the behavior of concrete, which does not exhibit a well-defined yield point. It should be noted that the new endochronic plasticity theory considered herein is substantially different from those versions of the older theory used to develop the concrete models described in References 5, 6, and 27. Proper closure of hysteresis loops is guaranteed in the present theory,<sup>(21)</sup> so that artifices, such as the jump-kinematic hardening introduced into the concrete model described in Reference 27, are not required. Some of the basic inelastic response features of this new theory have recently been discussed by Trangenstein and Read<sup>(25)</sup> and Murakami and Read.<sup>(26)</sup>

The purpose of the present report is to formulate an endochronic plasticity theory for plain concrete, based upon the general framework described in Reference 21, and to explore the capabilities of this new theory to predict the wide range of experimental results for complex multi-axial load paths reported in Reference 17. For this purpose, the model is first fit to a small subset of the data, and then exercised around a variety of different non-standard stress paths not used in fitting the model. It is shown that the model can successfully predict the nonlinear behavior of concrete under these complex loading conditions. This appears to provide strong indication that the present model has captured the basic constitutive characteristics of plain concrete quite well.

It should be noted that the scope of the present model is currently limited to stress levels in plain concrete that do not produce significant cracking. The model is isotropic and therefore incapable of describing stress-induced anisotropy produced by significant microcracking with preferred orientation. In many practical applications, this limitation may not prove to be overly

restrictive, since there are obviously many instances where a plain concrete structure is driven into the nonlinear regime but not to the point where substantial cracking occurs.

## SECTION 2

### THERMODYNAMIC FOUNDATIONS OF THEORY

Endochronic plasticity is founded on the theory of irreversible thermodynamics of internal variables. The foundations have been laid in detail elsewhere (see Ref. 21, for example) and will not be elaborated upon here. For the sake of completeness, however, we begin by recalling the basic equations.

#### 2.1 THERMODYNAMIC RELATIONS.

It is stipulated at the outset that concrete is macroscopically homogeneous and isotropic even though at the local level it is highly heterogeneous and anisotropic. Its mechanical response to strain (or stress) is also highly dissipative and therefore inelastic. In the thermodynamic formulation, interior dissipative mechanisms are formally represented by internal variables. Isotropy permits the separation of such mechanisms into deviatoric and hydrostatic ones, represented respectively by the internal variables  $q_r$  and  $p_r$ , where  $q_r$  are tensors of second order and  $p_r$  are scalars. In the context of small deformation theory,  $\psi$ , the free energy of deformation, is quadratic in the strain tensor and the internal variables and can therefore be partitioned in the case of isotropic materials into its deviatoric and hydrostatic parts. Thus

$$\psi = \psi_D + \psi_H \quad (2.1)$$

Specifically

$$\psi_D = \psi_D(\underline{\varepsilon}, g_r) \quad (2.2)$$

$$\psi_H = \psi_H(\varepsilon, p_r) \quad (2.3)$$

where  $\underline{\varepsilon}$  is the deviatoric part of the strain tensor  $\underline{\varepsilon}$  and  $\varepsilon$  is the hydrostatic part. Thus

$$\underline{\varepsilon} = \underline{\varepsilon} + \underline{I} \varepsilon \quad (2.4)$$

where  $\underline{I}$  is the unit matrix. It has been shown that in the case of materials which behave elastically at the onset of unloading or reloading (points of reversal in the sign of the strain rate)  $\psi_D$  can be further partitioned into an elastic and plastic part such that

$$\psi_D = \psi_D^e + \psi_D^p \quad (2.5)$$

where

$$\psi_D^e = \psi_D^e(\underline{\varepsilon}^e) \quad (2.6)$$

$$\psi_D^p = \psi_D^p(\underline{\varepsilon}^p, g_r) \quad (2.7)$$

and

$$d\underline{\varepsilon}^e = \frac{d\underline{\varepsilon}}{2\mu} \quad (2.8)$$

$$\underline{\varepsilon}^p = \underline{\varepsilon} - \underline{\varepsilon}^e ,$$

$\underline{s}$  is the deviatoric stress tensor and  $\mu$  is the elastic shear modulus. In a similar fashion

$$\psi_H = \psi_H^e + \psi_H^p \quad (2.9)$$

where

$$\psi_H^e = \psi_H^e(\epsilon) \quad (2.10)$$

$$\psi_H^p = \psi_H^e(\epsilon^p, p_r) \quad (2.11)$$

and

$$d\epsilon^e = \frac{d\sigma}{K} \quad (2.12)$$

$$\epsilon^p = \epsilon - \epsilon^e \quad (2.13)$$

$\sigma$  is the hydrostatic stress and  $K$  is the elastic bulk modulus. In parallel to Eq. (2.4)

$$g = \underline{s} + \frac{1}{K}\sigma \quad (2.14)$$

The topological interpretation of the above partitioning in the deviatoric case is given in Figure 1. The same interpretation applies to the hydrostatic case.

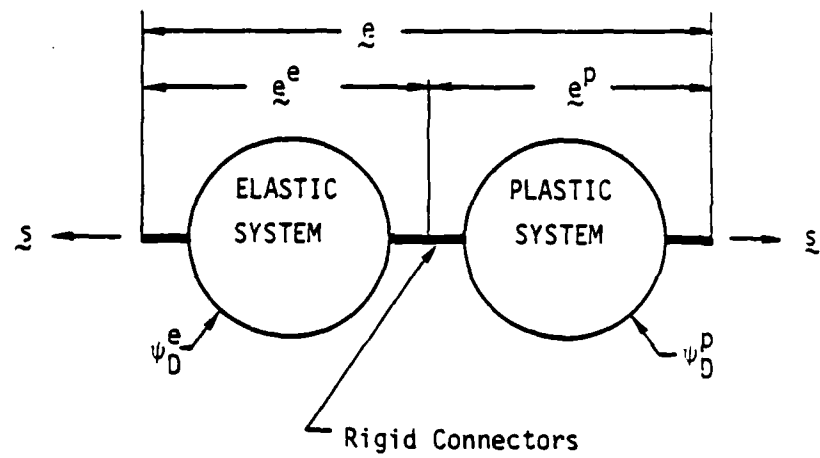


Figure 1. An elastic system and a plastic system in series.

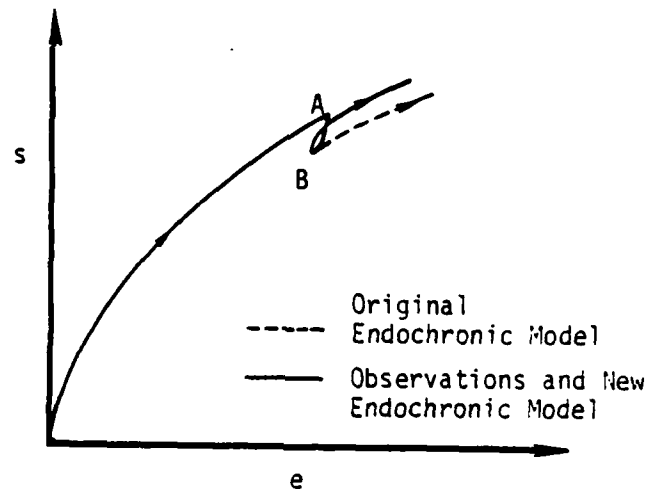


Figure 2. Elastic response at unloading and reloading.

The thermodynamic relations that apply are the following: (21)

$$\xi = \frac{\partial \psi_D^P}{\partial \underline{\epsilon}^P} \quad (2.15)$$

$$-\frac{\partial \psi_D^P}{\partial g_r} dg_r > 0 \quad , \quad ||dg_r|| < 0 \quad (2.16)$$

$$\sigma = \frac{\partial \psi_H^P}{\partial \epsilon^P} \quad (2.17)$$

$$-\frac{\partial \psi_H^P}{\partial p_r} dp_r > 0 \quad , \quad |dp_r| > 0 \quad (2.18)$$

Also

$$\xi = \frac{\partial \psi_D^e}{\partial \underline{\epsilon}^e} \quad (2.19)$$

$$\sigma = \frac{\partial \psi_H^e}{\partial \epsilon^e} \quad (2.20)$$

The above equations are obtained by applying the theory of irreversible thermodynamics to each individual system in Figure 1. Strict interpretation of the topological arrangement suggests that  $\psi_D^P$  cannot depend on  $\underline{\epsilon}^e$  and conversely  $\psi_D^e$  cannot\* depend on  $\underline{\epsilon}^P$ .

---

\*. However, in the actual material, internal changes associated with the plastic strain may affect the elastic moduli  $\mu_e$  and  $K_e$  and thus render  $\psi_D^P$  and  $\psi_H^e$  dependent of  $\underline{\epsilon}^P$  and  $\epsilon^P$ .

We note again that the free energies all have quadratic forms which have been shown to be reducible to the canonical forms given below

$$\psi_D^e = \mu_e \left| \epsilon^e \right|^2 \quad (2.21)$$

$$\psi_D^p = \frac{1}{2} \sum \mu_r \left| \epsilon^p - g_r \right|^2 \quad (2.22)$$

$$\psi_H^e = \frac{1}{2} K_e (\epsilon^e)^2 \quad (2.23)$$

$$\psi_H^p = \frac{1}{2} \sum K_r (\epsilon^p - p_r)^2 \quad (2.24)$$

It is physically appealing to introduce at this juncture the concept of internal forces  $Q_r$  and  $P_r$  such that

$$Q_r = - \frac{\partial \psi_D^p}{\partial g_r} \quad (2.25)$$

$$P_r = - \frac{\partial \psi_H^p}{\partial p_r} \quad (2.26)$$

It has been shown in previous work that  $q_r$  and  $p_r$  represent internal displacements either in terms of assemblies of mechanical models<sup>(21)</sup>, slip in crystals<sup>(31)</sup> or motion of atoms grouped together in terms of specific energy states<sup>(32)</sup>. Then in view of Eqs. (2.16) and (2.25) on one hand and Eqs. (2.17) and (2.26) on the other,

$$Q_r \cdot dg_r > 0 \quad , \quad ||dg_r|| > 0 \quad (2.27)$$

$$P_r dp_r > 0 \quad , \quad |dp_r| > 0 \quad (2.28)$$

The above equations are a statement to the fact that the increment of work done by an internal force is always positive, unless the associated internal variable is constant in which case the increment of work is zero.

## 2.2 EVOLUTION EQUATIONS.

Inequalities (2.27) and (2.28) may be written in the alternative "rate" form

$$Q_r \cdot \dot{g}_r > 0 \quad (2.29)$$

$$P_r \dot{p}_r > 0 \quad (2.30)$$

where a superposed dot indicates differentiation with respect to time.

In linear time-dependent systems

$$Q_r = b_r^{(1)} \dot{g}_r \quad (2.31)$$

$$P_r = b_r^{(2)} \dot{p}_r \quad (2.32)$$

The above equations may be viewed as "internal constitutive equations," or "rate equations" because they relate the internal forces

(linearly) to the rate of change of the internal displacements. In traditional thermodynamics they are regarded as the "Onsager Relations" since they relate (linearly) the dissipative (internal) forces to the "fluxes." Note that they satisfy the thermodynamic inequalities (2.29) and (2.30) if

$$b_r^{(1)} > 0 \quad , \quad b_r^{(2)} > 0 \quad (2.32 \text{ and } 2.33)$$

for all  $r$ .

We observe that Eqs. (2.31) and (2.32) in conjunction with Eqs. (2.25) and (2.26) give the "evolution equations"

$$\frac{\partial \psi_D^P}{\partial g_r} + b_r^{(1)} \dot{g}_r = 0 \quad (2.34)$$

$$\frac{\partial \psi_H^P}{\partial p_e} + b_r^{(2)} \dot{p}_r = 0 \quad (2.35)$$

Equations (2.22) and (2.24) in conjunction with Eqs. (2.34) and (2.35) respectively give linear differential equations in  $g_r$  and  $p_r$  from which these can be calculated if one knows the history of plastic strain. Specifically these equations are:

$$\mu_r g_r + b_r^{(1)} \dot{g}_r = \mu_r \epsilon^P \quad (2.36)$$

$$K_r p_r + b_r^{(2)} \dot{p}_r = K_r \epsilon^P \quad (2.37)$$

These may also be given in terms of the internal forces  $Q_r$  and  $P_r$  upon use of Eqs. (2.25) and (2.26). Thus when  $\mu_r$  and  $K_r$  are constant,

$$\frac{\mu_r}{b_r^{(1)}} Q_r + \frac{dQ_r}{dt} = \mu_r \frac{d\epsilon^P}{dt} \quad (2.38)$$

$$\frac{K_r}{b_r^{(2)}} P_r + \frac{dP_r}{dt} = K_r \frac{d\epsilon^P}{dt} \quad (2.39)$$

### 2.3 THE NOTION OF INTRINSIC TIME.

In materials which are history dependent but rate-indifferent "newtonian" time is not a proper time scale for the formulation of evolution equations. The difficulty lies in the fact that in such materials the stress is a function of the deformation path but not of the rate at which the path is traversed. This fact was the basis of the idea proposed by the first author in 1971<sup>(28)</sup> that every material posses an intrinsic time scale with respect to which the evolution equations of such material should be formulated.

With reference to System 2 in Figure 1, we note that the deformation of that system is defined by the plastic strain tensor  $\epsilon^P$ . We define therefore a path in the plastic strain space whose length increment  $dz$  is given by the relation

$$dz^2 = P_{ijkl} d\epsilon_{ij}^P d\epsilon_{kl}^P \quad (2.40)$$

We stipulate that the tensor  $\underline{P}$  is isotropic. Thus it admits the representation

$$P_{ijkl} = k_1^2 \delta_{ij} \delta_{kl} + k_2^2 \delta_{ik} \delta_{jl} \quad (2.41)$$

which when combined with Eq. (2.40) admits the result

$$dz^2 = k_1^2 d\epsilon_{kk}^P d\epsilon_{ii}^P + k_2^2 d\epsilon_{ik}^P d\epsilon_{ik}^P \quad (2.42)$$

or, within an immaterial multiplicative constant,

$$dz^2 = \left| |d\underline{\epsilon}^P| \right|^2 + k^2 |d\epsilon^P|^2 \quad (2.43)$$

where  $\left| |d\underline{\epsilon}^P| \right|^2 = d\epsilon_{ij}^P d\epsilon_{ij}^P$ ,  $|d\epsilon^P|$  is the absolute value of  $d\epsilon^P$  and  $k$  is a material parameter.

If one retains the form of the evolution Eqs. (2.31) and (2.32) and, therefore, (2.34) and (2.35) and regards  $dz$  in Eq. (2.40) as an intrinsic time measure then in terms of this time scale  $z$  Eqs. (2.34) and (2.35) become

$$\frac{\partial \psi_D^P}{\partial g_r} + b_r^{(1)} \frac{dg_r}{dz} = 0 \quad (2.44)$$

$$\frac{\partial \psi_H^P}{\partial p_r} + b_r^{(2)} \frac{dp_r}{dz} = 0 \quad (2.45)$$

These two Eqs. lead to the counterparts of Eqs. (2.38) and (2.39) as shown below.

$$\frac{\mu_r}{b_r^{(1)}} \dot{q}_r + \frac{dq_r}{dz} = \mu_r \frac{d\epsilon^p}{dz} \quad (2.46)$$

$$\frac{K_r}{b_r^{(2)}} P_r + \frac{dP_r}{dz} = K_r \frac{d\epsilon^p}{dz} \quad (2.47)$$

Equations (2.15) and (2.17) give the relations between the stresses and the internal forces. Specifically in view of Eqs. (2.22) and (2.24)

$$\underline{s} = \sum_r \underline{q}_r \quad (2.48)$$

$$\sigma = \sum_r P_r \quad (2.49)$$

Equations (2.43) and (2.46 - 2.49), together with Eqs. (2.8) and (2.12), provide a complete constitutive description of a dissipative, rate-independent (plastic) material, subject to the above stipulations.

#### 2.4 INTEGRAL FORM OF THE EQUATIONS

In general the resistance tensors  $b_r^{(1)}$  and  $b_r^{(2)}$  are not constant but depend on other variables associated with the deformed state of a material. A propos of this eventuality we set

$$b_r^{(1)} = F_s b_{or}^{(1)} \quad (2.50)$$

$$b_r^{(2)} = F_H b_{or}^{(2)} \quad (2.51)$$

where  $F_s$  and  $F_H$  are specified on the basis of the observed response of a particular material. This question will be dealt with in the next section. Let

$$a_r = \frac{\mu_r}{b_{or}^{(1)}} \quad (2.52)$$

$$\lambda_r = \frac{K_r}{b_{or}^{(2)}} \quad (2.53)$$

where  $b_{or}^{(1)}$  and  $b_{or}^{(2)}$  are constants.

Further we define intrinsic time scales  $z_s$  and  $z_H$  by the relation

$$dz_s = \frac{dz}{F_s} \quad (2.54a)$$

$$dz_H = \frac{dz}{kF_H} \quad (2.54b)$$

where  $k$  in Eq. (2.54) is the same as the parameter  $k$  appearing in the definition of intrinsic time given by Eq. (2.43). The appearance of  $k$  in Eq. (2.54) is not purely formal but has the advantage that the pure hydrostatic response so derived is independent of  $k$ , as will be shown later.

In the light of the above definitions, Eqs. (2.46) and (2.47) become

$$a_r Q_r + \frac{dQ_r}{dz_s} = \mu_r \frac{de^P}{dz_s} \quad (2.55)$$

$$\lambda_r P_r + \frac{dP_r}{dz_H} = K_r \frac{d\epsilon^P}{dz_H} \quad (2.56)$$

Let the reference configuration be one at which  $z_H = z_s = 0$ . We define a "natural configuration" as one at which  $Q_r(0) = 0$ ,  $P_r = 0$ . There are, of course, configurations (initially strained or arising because of a nonequilibrium thermomechanical reference state) in which  $Q_r(0) \neq 0$ ,  $P_r(0) \neq 0$ . Thus for greater generality we set

$$Q_r(0) = Q_r^0, \quad P_r(0) = P_r^0 \quad (2.57a,b)$$

Equations (2.55) and (2.56) may now be integrated subjected to the initial conditions (2.57a,b) to give

$$Q_r = Q_r^0 e^{-a_r z_s} + \mu_r \int_0^{z_s} e^{-a_r(z_s-z')} \frac{de^P}{dz'} dz' \quad (2.58a)$$

$$P_r = P_r^0 e^{-\lambda_r z_H} + K_r \int_0^{z_H} e^{-\lambda_r(z_H-z')} \frac{d\epsilon^P}{dz'} dz' \quad (2.58b)$$

Use of Eqs. (2.48) and (2.49) gives the stress in terms of convolution integrals of the plastic strain history as follows

$$\underline{s} = \sum_r \underline{q}_r^0 e^{-a_r z_s} + \int_0^{z_s} \rho(z_s - z') \frac{\partial \epsilon^p}{\partial z'} dz' \quad (2.59)$$

$$\sigma = \sum_r p_r^0 e^{-\lambda_r z_H} + \int_0^{z_H} \phi(z_H - z') \frac{\partial \epsilon^p}{\partial z'} dz' \quad (2.60)$$

where

$$\rho = \sum_r \mu_r e^{-a_r z_s} \quad (2.61)$$

$$\phi = \sum_r K_r e^{-\beta_r z_H} \quad (2.62)$$

The condition that  $\underline{s} = 0$  in the reference state requires that

$$\sum_r \underline{q}_r^0 = 0 \quad (2.63)$$

whereas the condition that  $\sigma = 0$  in the reference state requires that

$$\sum_r p_r^0 = 0 \quad (2.64)$$

If the reference state is a "natural" state, then

$$\xi = \int_0^{z_s} \rho(z_s - z') \frac{d\epsilon^p}{dz'} dz' \quad (2.65)$$

$$\sigma = \int_0^{z_H} \phi(z_H - z') \frac{d\epsilon^p}{dz'} dz' \quad (2.66)$$

## 2.5 SINGULAR KERNELS.

It was shown by the first author<sup>(21)</sup> that if the kernel  $\rho(z_s)$  is weakly singular in the sense that  $\rho(0) = \infty$  but integrable,

$$\int_0^{z_s} \rho(z_s') dz_s' < \infty, \quad z_s < \infty \quad (2.67)$$

then the hysteresis loop of a material in the first quadrant of the stress-strain space is closed. It was also shown that the material response at unloading and reloading points is elastic in the sense of Figure 2. The reason for this is that

$$\left. \frac{d\tau}{d\gamma^p} \right|_A = \left. \frac{d\tau}{d\gamma^p} \right|_B = \left. \frac{d\tau}{d\gamma^p} \right|_C = \infty \quad (2.68)$$

because of the singularity of the kernel. The elastic response at these points is then the response of the elastic system of Figure 1.

In numerical computations the singular kernel is approximated by a Prony series as in Eq. (2.61), in which care is taken so that  $\rho(0)$ , where

$$\rho(0) = \sum_r \mu_r \quad , \quad (2.69)$$

is a very large number in the sense that

$$\rho(0) \gg \mu_e \quad (2.70)$$

where  $\mu_e$  is the elastic slope at the loading point A of Figure 2.

## SECTION 3

### SPECIFIC FORM OF THEORY FOR PLAIN CONCRETE

The application of endochronic plasticity to metals is facilitated by three assumptions which are quite realistic:

- (i) Under moderate hydrostatic stress,\* the hydrostatic response of metals is elastic.
- (ii) A constant moderate hydrostatic stress does not affect the mechanical response of a metal in shear.
- (iii) Shearing at constant hydrostatic stress does not induce a change in the hydrostatic strain.

In concrete the above assumptions are not realistic.

In reference to item (i) above, the hydrostatic behavior of concrete in compression is illustrated in Figure 3. It is initially convex becoming concave and asymptotically elastic. Upon unloading at A to a point B a significant amount of plastic strain,  $\epsilon_p$  results. There is obviously a great deal of hardening taking place, which affects dramatically the subsequent loading-unloading-reloading behavior as illustrated in Figure 3. While in metals hardening, in general, is the result of multiplication of dislocations, in concrete it is very much a function of compaction. In both cases however the agents of hardening are the resistance coefficients  $b^r$  and in this particular instance,  $b^r_{(2)}$ . Thus while in metals one achieves

---

\*. Of the order of the yield stress in tension.

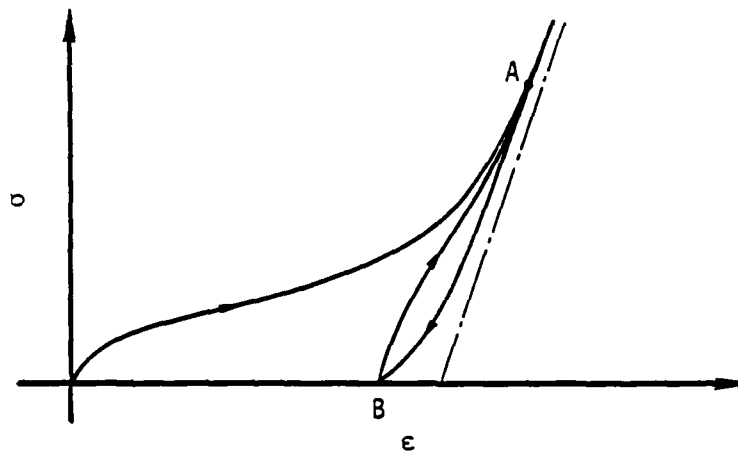


Figure 3. Typical response of plain concrete to pure hydrostatic compression.

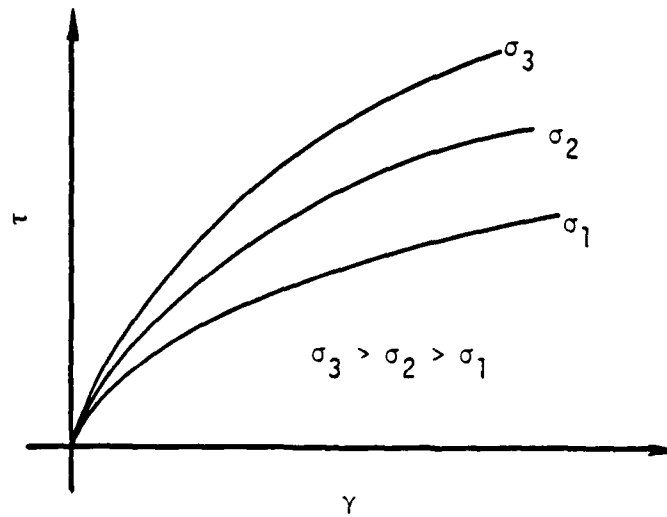


Figure 4. Shear response as a function of the hydrostatic compression.

hardening by letting  $b^r$  be an increasing function of  $z$ , in concrete, to account for the compaction effect in the hydrostat, we have set

$$b_{(2)}^r = b_{(2)}^r F_H(\epsilon^P) \quad (3.1)$$

where  $F_H$  is a monotonically increasing function of  $\epsilon^P$ .

In reference to item (ii), the shear response depends strongly on the existing level of hydrostatic stress. This effect is illustrated schematically in Figure 4 where the shear stress is plotted versus the shear strain under monotonic loading conditions and at various levels of constant hydrostatic stress. In regard to item (iii), the mechanical response of concrete shows strong shear-hydrostatic interaction in that shearing at constant hydrostatic stress produces a significant change in the hydrostatic strain and vice versa. As will be shown subsequently, endochronic plasticity accounts for this effect through the intrinsic time and specifically by virtue of the coupling constant  $k$  which appears in Eq. (2.43). Note that in materials which are plastically incompressible,  $d\epsilon^P = 0$ . In such materials shear-hydrostatic interaction is absent.

### 3.1 HYDROSTATIC RESPONSE.

Determination of the material functions  $\phi(z_H)$  and  $F_H(\epsilon^P)$ . It is assumed at the outset that the initial state is a natural state in which case the hydrostatic response is given by Eq. (2.66) which we write in the explicit form

$$\sigma = \int_0^{z_H} \phi(z_H - z') \frac{d\epsilon^P}{dz'} dz' \quad (3.2)$$

Under monotonic loading conditions, and in view of Eqs. (2.43) and (2.54), it follows that

$$\frac{d\epsilon^P}{dz_H} = F_H \quad (3.3)$$

Thus letting

$$dS_H = |d\epsilon^P| \quad (3.4)$$

it follows that

$$dz_H = \frac{k d\epsilon^P}{kF_H(\epsilon^P)} = \frac{dS_H}{F_H(\epsilon^P)} \quad (3.5)$$

Under monotonic straining conditions  $dz_H = d\epsilon^P$  hence

$$dS_H = \frac{d\epsilon^P}{F_H(\epsilon^P)} \quad (3.6)$$

Thus Eq. (3.2) becomes

$$\sigma = \int_0^{z_H} \phi(z_H - z') F_H(\epsilon^P) dz' \quad (3.7)$$

Two material functions, therefore, are necessary and sufficient to determine the hydrostatic response: the kernel  $\phi(z_H)$  and the hardening function  $F_H(\epsilon^P)$ .

### 3.1.1 The Hardening Function $F_H$ .

This function will be examined in reference to the hydrostatic stress-strain curve shown in Figure 5. The curve ON represents the stress response corresponding to  $F_H = 1$ . In the initial stage ( $\epsilon^P \leq OA$ )  $F_H$  is substantially linear. In the stage  $OA < \epsilon^P \leq OB$  it is substantially hyperbolic. In the final stage  $\epsilon^P > OB$   $\sigma \rightarrow \infty$  as  $\epsilon^P \rightarrow \epsilon_C^P$ , since there is a limiting material compressibility beyond which the material cannot be compressed no matter how high a stress  $\sigma$  is applied.

We shall take the position that

$$F_H = e^{\beta \epsilon^P} \quad (3.8)$$

which, in the range  $\epsilon^P \leq OA$ , we can write as

$$F_H = 1 + \beta \epsilon^P + O(\epsilon^P)^2 \quad (3.9)$$

The linear representation of  $F_H$  inherent in Eq. (3.9) affords an explicit method of determination of the value of  $\beta$  and the kernel  $\phi(z_H)$ .

### 3.1.2 Method of Analysis.

It follows from Eqs. (3.67) and (3.9) that

$$dz_H = \frac{d\epsilon^P}{1 + \beta \epsilon^P} \quad (3.10)$$

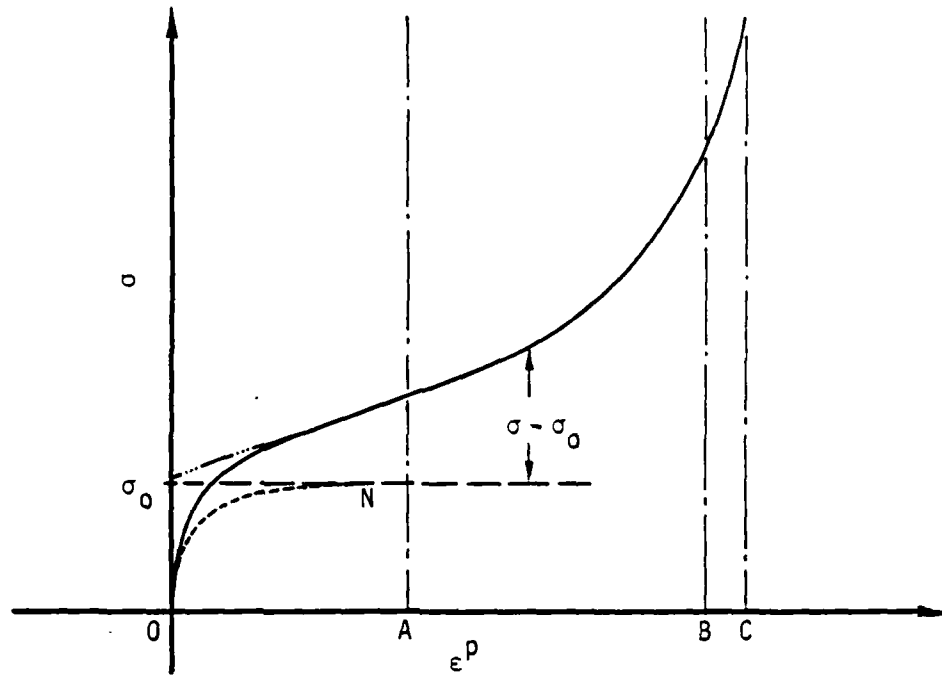


Figure 5. Pressure versus plastic volumetric strain for virgin hydrostatic compression.

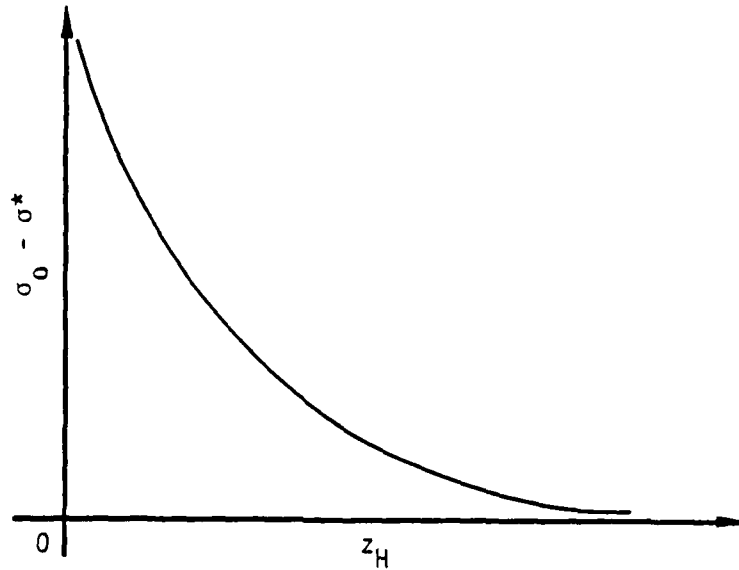


Figure 6. General form of the relationship between  $\sigma_0 - \sigma^*$  and  $z_H$ .

Hence

$$z_H = \frac{1}{\beta} \log(1 + \beta \epsilon^P) \quad (3.11)$$

or

$$\epsilon^P = \frac{1}{\beta} (e^{\beta z_H} - 1) \quad (3.12)$$

Thus

$$F_H = e^{\beta z_H} \quad (3.13)$$

Following, therefore, Eqs. (2.62) and (3.7)

$$\sigma = \sum_r \int_0^{z_H} K_r e^{-\lambda_r(z_H - z)} e^{\beta z} dz \quad (3.14)$$

or

$$\sigma = \sum_r K_r e^{-\lambda_r z_H} \left( \frac{1}{\lambda_r + \beta} \right) \left[ e^{(\lambda_r + \beta) z_H} - 1 \right] \quad (3.15)$$

Thus, if we define a stress  $\sigma^*$  such that

$$\sigma^* = \frac{\sigma}{F_H} = \frac{\sigma}{1 + \beta \epsilon^P} \quad (3.16)$$

it follows from Eq. (3.15) that

$$\sigma^* = \sum_r \frac{K_r}{\beta + \lambda_r} \left[ 1 - e^{-(\beta + \lambda_r)z_H} \right] \quad (3.17)$$

### 3.1.2 Determination of the Constants $K_r$ , $\lambda_r$ and $\beta$ .

To determine these constants we proceed as follows. The constant  $\beta$  is found from the straight line portion of the hydrostat given by the relation

$$\sigma = \sigma_0 (1 + \beta \epsilon^D) \quad (3.18)$$

where  $\sigma_0$  is the intercept shown in Figure 5.

The remaining constants are found by plotting  $\sigma_0 - \sigma^*$  versus  $z_H$  where  $z_H$  is given by Eq. (3.11). The plot is shown in Figure 6. It follows by virtue of Eq. (3.17) that

$$\sigma_0 - \sigma^* = \sum_r \frac{K_r}{\beta + \lambda_r} e^{-(\beta + \lambda_r)z_H} \quad (3.19)$$

Hence a Prony series representation of the curve  $\sigma_0 - \sigma^*$  versus  $z_H$  gives  $K_r/(\beta + \lambda_r)$  and  $\beta + \lambda_r$ . Since  $\beta$  is already known,  $K_r$  and  $\lambda_r$  are thus also known.

## 3.2 SHEAR RESPONSE.

The deviatoric part of the stress tensor (the shear response) is given by Eq. (2.65). Specifically

$$z = \int_0^{z_s} \rho(z_s - z'_s) \frac{d\epsilon^p}{dz'_s} dz'_s \quad (3.20)$$

where

$$dz^2 = \left| |d\epsilon^p| \right|^2 + k^2 (d\epsilon^p)^2 \quad (3.21a)$$

and

$$dz_s = \frac{dz}{F_s} \quad (3.21b)$$

in accordance with Eqs. (2.42) and (2.54). Thus two material functions,  $\rho(z_s)$  and  $F_s$  and the constant  $k$  are sufficient to determine the shear stress from the plastic strain history. It has been found experimentally that the failure stress of concrete in the  $\pi$ -plane depends on the prevailing hydrostatic stress and the direction of loading in the  $\pi$ -plane. To account for these two effects it is necessary that  $F_s$  depend on  $\sigma$  and the Lode angle  $\theta$ . Thus we set

$$F_s = F_s(\sigma, \theta) \quad (3.22)$$

subject to the normalization condition  $F_s(0,0) = 1$ .

### 3.2.1 The Kernel $\rho(z_s)$ .

The form of the function  $\rho(z_s)$  is found most conveniently by means of a pure shear test in the absence of hydrostatic stress. In this case

$$\sigma = 0, \theta = 0, \epsilon^P = 0, F_s = 1$$

If the non-vanishing stress component is  $\tau$  and the corresponding plastic strain component is  $\gamma^P$ , then in view of Eq. (3.21) we can write

$$\begin{aligned} dz &= \sqrt{2} |d\gamma^P| \\ dz_s &= dz \end{aligned} \tag{3.23}$$

Thus using Eq. (3.20)

$$\tau = \frac{1}{\sqrt{2}} M(\sqrt{2}\gamma^P) \tag{3.24}$$

where

$$M(x) = \int_0^x \rho(z') dz' \tag{3.25}$$

for all finite  $x$ . Thus

$$\frac{d(\sqrt{2}\tau)}{d(\sqrt{2}\gamma^P)} = \frac{d\tau}{d\gamma^P} = \rho(\sqrt{2}\gamma^P) \tag{3.26}$$

Thus, if one plots  $\sqrt{2}\tau$  versus  $\sqrt{2}\gamma^P$ , the slope of the curve is the kernel function  $\rho(x)$  where  $x = \sqrt{2}\gamma^P$ .

### 3.2.2 The Function $F_S$ .

The determination of the form of  $F_S$  and the value of  $k$  is more complex due to the strong coupling between the hydrostatic and deviatoric responses brought about by the presence of  $k$  in Eq. (3.21).

Consider for instance a shear stress field in the presence of a constant hydrostatic stress. More precisely a hydrostatic stress field is applied until  $\sigma = \sigma_1$ , whereupon  $\sigma$  is held constant at  $\sigma_1$  and a shear stress field  $\tau$  is then applied, so that while  $\tau$  is being applied the total stress field is of the form

$$\underline{\sigma} = \begin{pmatrix} \sigma_1 & \tau & 0 \\ \tau & \sigma_1 & 0 \\ 0 & 0 & \sigma_1 \end{pmatrix} \quad (3.27)$$

One first notes that the application of shear stress changes the hydrostatic plastic strain by virtue of Eq. (3.2). To see this we invert Eq. (3.2) i.e., express  $\epsilon^P$  in terms of the history of  $\sigma$ .

$$\epsilon^P = \int_0^{z_H} L(z_H - z_H') \frac{d\sigma}{dz_H'} dz_H' \quad (3.28)$$

where  $L$  is related to  $\phi$  by the integral equation

$$\int_0^z \phi(z - z') \frac{dL'}{dz'} dz' = H(z) \quad (3.29)$$

where  $H(z)$  is the Heaviside step function. Let  $z_H = z_H^0$  at the termination of the hydrostatic test, i.e., at  $\sigma = \sigma_1$ . Then in view of Eq. (3.28)

$$\epsilon^P = \int_0^{z_H^0} L(z_H - z_H^0) \frac{d\sigma}{dz_H} dz_H \quad (3.30)$$

since  $\frac{d\sigma}{dz_H} = 0$  when  $z_H > z_H^0$ .

Since the application of shear stress will cause a change in the shear strain,  $z$  will change by virtue of Eq. (3.21), and so will  $z_H$  by virtue of Eq. (2.54). Thus the integral on the righthand side of Eq. (3.30) will change and hence so will  $\epsilon^P$ . Thus, in the presence of hydrostatic stress,  $dz$  is no longer given by Eq. (3.23) but by Eq. (3.21), which is influenced by the value of  $k$ .

The problem simplifies somewhat and becomes amenable to analysis if one adopts a simpler form of the hydrostat. With reference to Eq. (3.2), the kernel  $\phi(z_H)$  decays with sufficient rapidity to be approximated by a Dirac  $\delta$  function. Thus we set

$$\phi(z_H) = K_0 \delta(z_H) \quad (3.31)$$

in which case by virtue of Eq. (3.2), it follows that

$$\sigma = K_0 \frac{d\epsilon^P}{dz_H} \quad (3.32)$$

Specifically under purely hydrostatic monotonic loading conditions Eq. (3.3) applies in which case

$$\sigma = K_0 (1 + \beta \epsilon^P) \quad (3.33)$$

by virtue of Eqs. (3.9) and (2.43). Equation (3.33) is then basically that of a plastic linearly hardening model. In particular if  $\sigma_1$  is on the linear part of the hydrostatic stress-strain curve, Eqs. (3.33) is certainly adequate.

It follows from Eqs. (3.32) that

$$d\epsilon^P = \frac{\sigma_1}{K_0} dz_H \quad (3.34)$$

where  $\sigma_1$  is the (constant) value of the hydrostatic stress during shearing.

Adopting the sign convention commonly used in civil engineering whereby  $\sigma$  and  $\epsilon^P$  are positive when compressive, we note, in view of Eq. (3.34), that  $d\epsilon^P$  will be positive, and hence the compressive strain will increase, during shearing.

In view of the above observations we introduce the following notation

$$d\zeta_s = \left| |d\epsilon^P| \right|, \quad d\zeta_H = |d\epsilon^P| \quad (3.35a.b)$$

Thus, because of Eq. (2.43),

$$dz^2 = d\zeta_s^2 + k^2 d\zeta_H^2 \quad (3.36)$$

We now combine Eqs. (2.54) and (3.32) to obtain

$$\sigma = kK_0(1 + \beta\zeta_H) \frac{d\zeta_H}{dz} \quad (3.37)$$

where use was made of Eq. (3.33), (3.35b) and the fact that during the hydrostatic as well as the shearing processes  $d\epsilon^P > 0$ . Equations (3.36) and (3.37) combine to give the result

$$dz \left\{ 1 - \left[ \frac{\sigma_1}{K_0(1 + \beta\zeta_H)} \right]^2 \right\}^{1/2} = d\zeta_s \quad (3.38)$$

Now let  $\zeta_H^P (= \epsilon^P)$  be the value of  $\epsilon^P$  at the completion of the purely hydrostatic loading so that

$$\zeta_H = \zeta_H^P + \zeta_H^S \quad (3.39)$$

where  $\zeta_H^S$  is the hydrostatic strain induced by shear loading at constant pressure. Also let

$$z = z' + y \quad (3.40)$$

where  $z'$  is the value of  $z$  at the completion of the purely hydrostatic loading. Without going into extensive analytical detail Eqs. (3.36), (3.37) and (3.38) combine to give the following results:

$$\frac{d\zeta_s}{dy} = \left( \frac{2ay}{1 + 2ay} \right)^{1/2} \quad (3.41)$$

where

$$a = \frac{K_0 \beta}{k \sigma_1} \quad (3.42)$$

and

$$\zeta_s = \frac{1}{2a} \left\{ x \sqrt{x^2 - 1} - \log \left( x + \sqrt{x^2 - 1} \right) \right\} \quad (3.43)$$

where

$$x = 1 + \frac{K_0 \beta}{\sigma_1} S_H^s \quad (3.44)$$

Relations (3.41) and (3.43) will prove useful in determining the form of  $F_s$  and the value of  $k$ .

We now return to the question of the shear stress response to increasing shear strain in the presence of constant pressure, i.e., to the case where the stress field is given by Eq. (3.27). In view of Eq. (3.20), we can write

$$\tau = \int_0^{z_s} \rho(z_s - z'_s) \frac{d\gamma^p}{dz'_s} dz'_s \quad (3.45)$$

However,  $\gamma^P = 0$  during pure hydrostatic loading, i.e., in the range  $0 \leq z_s \leq z'_s$ . Thus, if we set  $w = z_s - z'_s$  and recall Eq. (3.45), it follows that

$$\tau = \int_0^w \rho(w - w') \frac{d\gamma^P}{dw'} dw' \quad (3.45a)$$

We note that

$$\frac{d\gamma^P}{dw'} = \frac{d\gamma^P}{d\zeta_s} \frac{d\zeta_s}{dw} = \frac{1}{\sqrt{2}} \frac{d\zeta_s}{dw} \quad (3.46)$$

in view of Eq. (3.35a). Therefore, as a result of Eqs. (3.21b) and (3.41)

$$\frac{d\zeta_s}{dw} = F_s \left( \frac{2aF_s w}{1 + 2aF_s w} \right)^{1/2} \quad (3.47)$$

where in this case

$$F_s = F_s(\sigma, 0) \quad (3.48)$$

i.e.,  $F_s$  is constant during the shearing process.

Thus as a result of Eqs. (3.45a), (3.46) and (3.47)

$$\tau = \frac{F_s}{\sqrt{2}} \int_0^w \rho(w - w') \left( \frac{2aF_s w}{1 + 2aF_s w} \right)^{1/2} dw' \quad (3.49)$$

It is shown in Appendix I that

$$\lim_{z \rightarrow \infty} \int_0^w \rho(z - z') \left( \frac{2aF_s z'}{1 + 2aF_s z'} \right)^{1/2} dz' = M_\infty \quad (3.50)$$

where  $M(z)$  is given by Eq. (3.25) and  $M_\infty = M(\infty) < \infty$ . Hence, denoting the asymptotic value of the shear stress by  $\tau_\infty$  it follows from Eqs. (3.49) and (3.50) that

$$\tau_\infty = \frac{F_s}{\sqrt{2}} M_\infty \quad (3.51)$$

During shearing at zero pressure one may set  $F_s = 1$ . Thus

$$\frac{\tau_\infty(\sigma_1)}{\tau_\infty(0)} = F_s \quad (3.52)$$

Equation (3.52) determines the form of  $F_s$  under constant  $\theta$ . Keeping  $\sigma$  constant and performing shearing tests each at a different value of  $\theta$  one is able to determine the form of functional dependence of  $F_s$  on  $\theta$ .

### 3.2.3 Determination of the Kernel $\rho(w)$ in the Presence of Pressure.

In the course of the development of the theory in conjunction with the experimental data of Scavuzzo, *et al.*<sup>(17)</sup> it transpired that

all shear experiments were performed in the presence of pressure i.e., under conditions where  $\sigma_1 \neq 0$ . In this event Eq. (3.24) no longer applies and Eq. (3.49) must be used for the determination of  $\rho(w)$ . To this end we set  $F_s = 1$  at a reference pressure  $\sigma_R$ , which is the one we use in the determination of  $\rho(w)$ , and which must lie on the straight line segment of the hydrostat to ensure that Eq. (3.49) is applicable. Thus setting  $F_s = 1$  in Eq. (3.49) we obtain the following relation for  $\tau$ :

$$\tau = \frac{1}{\sqrt{2}} \int_0^y \rho(y - y') \left( \frac{2ay'}{1 + 2ay'} \right)^{1/2} dy' \quad (3.53)$$

where as before

$$a = \frac{K_0 \beta}{K \sigma_R} \quad (3.54)$$

and since  $y = w$  when  $F_s = 1$ .

Thus given  $\tau$  (which is measured experimentally) and  $a$ , the task at hand is to solve the integral equation (3.53) and thus obtain the functional form of  $\rho$ .

Before we proceed with the solution we take care to note that  $\tau$  is measured as a function of the shear strain  $\gamma$  and is therefore reducible to a function of the plastic strain  $\gamma^P$ . In the presence of monotonic shearing conditions and in view of Eq. (3.35a)

$$d\zeta_s = \sqrt{2} d\gamma^P \quad (3.55)$$

Furthermore, since at the initiation of the shear test  $\zeta_s = 0$ , it follows that

$$\zeta_s = \sqrt{2} \gamma^p \quad (3.56)$$

Thus in view of the relation between  $\zeta_s$  and  $y$  (Eq. 3.44),  $\zeta_s$  can be expressed as a function of  $y$ . Thus the function on the lefthand side of Eq. (3.53) is a known function of  $y$ .

#### 3.2.4 Numerical Procedure for Determining the Kernel Function $\rho(z_s)$ .

We proceed to give a numerical solution to the equation

$$\tau(y) = \int_0^y \rho(y - y') g(y') dy' \quad (3.57)$$

where the object is to determine  $\rho(y)$  given the functions  $\tau(y)$  and  $g(y)$ . Note that Eq. (3.53) is a particular case of Eq. (3.57) where

$$g(y) = \frac{1}{\sqrt{2}} \left( \frac{2ay}{1 + 2ay} \right)^{1/2} \quad (3.58)$$

Let  $y_n$  be a generic value of the variable  $y$ . We divide the interval  $[0, y]$  into suitably small equal subintervals  $\Delta$  such that

$$y_n = n\Delta \quad (3.59)$$

The integral on the righthand side of Eq. (3.57) can then be written in the form

$$\begin{aligned} \tau(y_n) = \tau_n = & \int_0^{\Delta} \rho(y_n - y') g(y') dy' + \dots \\ & \dots + \int_{(n-1)\Delta}^{n\Delta} \rho(y_n - y') g(y') dy' \end{aligned} \quad (3.60)$$

or

$$\tau_n = \sum_{r=1}^n g_r \{M[(n-r+1)\Delta] - M[(n-r)\Delta]\} \quad (3.61)$$

where  $y$  virtue of the mean value theorem

$$g_r = g(y_r^*) \quad , \quad (3.62)$$

$$(r-1)\Delta \leq y_r^* \leq r\Delta \quad (3.63)$$

and

$$M(r\Delta) = \int_0^{r\Delta} \rho(y') dy' \quad (3.64)$$

The quantity  $g_r$  may be determined to the required degree of accuracy by making the interval  $\Delta$  sufficiently small.

In consequence, we have the relations

$$\begin{aligned}\tau_1 &= \Delta g_1 M(\Delta) \\ \tau_2 &= \Delta g_1 M(2\Delta) + \Delta g_2 M(\Delta)\end{aligned}\tag{3.65}$$

$$\tau_n = \Delta g_1 M(n\Delta) + \Delta g_2 M[(n-1)\Delta] + \dots + \Delta g_n M(\Delta)$$

where

$$\Delta g_r = g_r - g_{r-1}\tag{3.66}$$

This is a system of a linear simultaneous equations in  $M(\Delta)$ ,  $M(2\Delta)$  ...  $M(n\Delta)$ . Since the  $\Delta g_r$  are known, then knowing  $\tau_1, \tau_2 \dots \tau_n$  allows one to determine  $M(r\Delta)$ ,  $r = 1, 2 \dots n$ , by successive substitution. The following algorithm applies:

If

$$\bar{\tau}_n = \sum_{m=1}^{n-1} \Delta g_{n+1-m} M(m\Delta)\tag{3.67}$$

then

$$M(r\Delta) = \frac{\tau_n - \bar{\tau}_n}{\Delta g_1}\tag{3.68}$$

Knowledge of  $M(y)$  thus allows the determination of  $\rho(y)$  since

$$\rho(y) = \frac{dM(y)}{dy}\tag{3.69}$$

## SECTION 4

### EVALUATION OF MODEL PARAMETERS FROM PLAIN CONCRETE DATA

In the preceding section, a specific form of the general endochronic model described in Section 2 was given for plain concrete, and a basic approach was given for determining the material constants in the model from experimental data. In this section, the model is applied specifically to the data on plain concrete recently reported by Scavuzzo, *et al.*<sup>(17)</sup> The model is first fit to a small subset of the data, and the resulting model is then proof-tested against the data from a wide variety of the complex strain path tests not used in fitting the model. The predictive capabilities of the model are demonstrated.

#### 4.1 DETERMINATION OF MODEL PARAMETERS.

Only a small subset of the data reported by Scavuzzo, *et al.*<sup>(17)</sup> is needed to determine the values of the model parameters; for this purpose, pure hydrostatic compression data, data on the response to shear at several different fixed hydrostatic pressures and triaxial failure data at various confining pressures proves sufficient. Details of the manner in which this can be accomplished are given below.

##### 4.1.1 Hydrostatic Parameters.

The most extensive virgin pure hydrostatic compression curve reported by Scavuzzo, *et al.*<sup>(17)</sup> is depicted by the dotted line in Figure 7, covering the range of pressures up to nearly 14 ksi. Shown also in Figure 7 by the solid line is the virgin hydrostatic compression curve actually used in determining the model parameters.

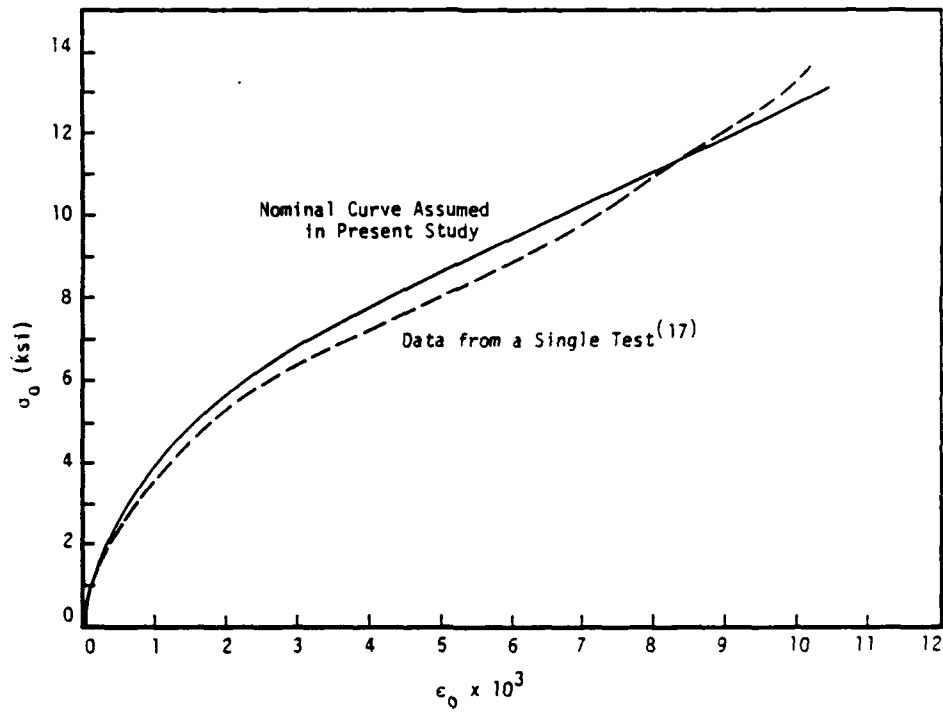


Figure 7. Octahedral normal stress versus octahedral normal strain for virgin hydrostatic compression.

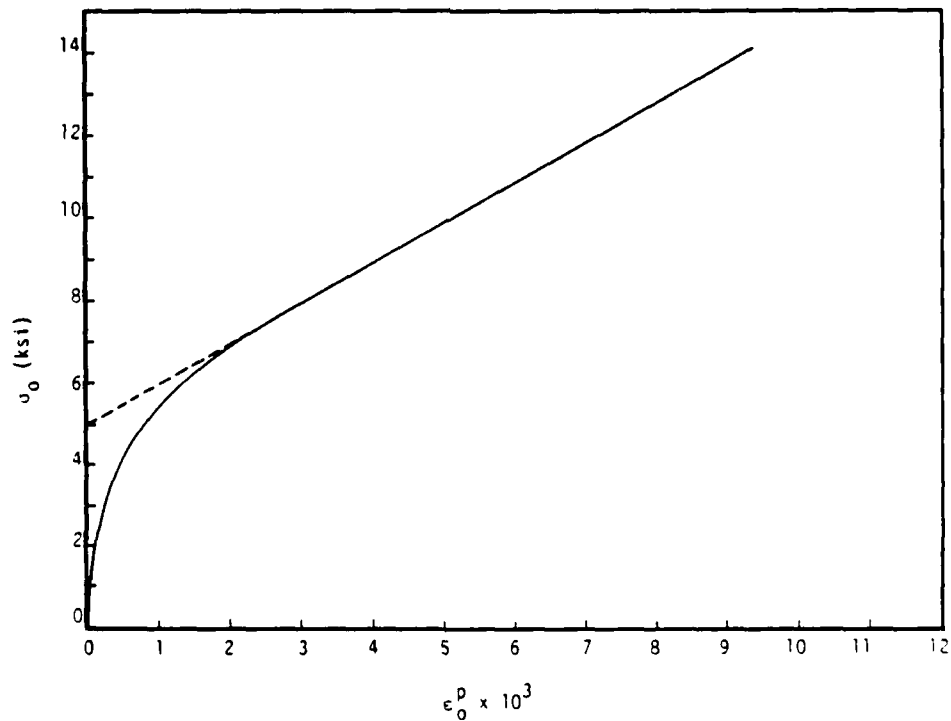


Figure 8. Octahedral normal stress versus plastic octahedral normal strain for virgin hydrostatic compression.

An examination of the virgin pure hydrostatic compression legs of many of the complex strain path tests revealed that the dotted curve in Figure 7 was probably too soft. Therefore, from this examination, the curve shown by the solid line was constructed and appears to provide a more accurate portrayal of the normal virgin hydrostatic behavior; the linearization of the upper portion of the hydrostatic curve was felt to be justified in view of the fact that none of the complex stress path tests reported by Scavuzzo, *et al.* exceeded hydrostatic pressures of 12 ksi. Note that the curves shown in Figure 7 are expressed in terms of octahedral normal stress  $\sigma_o$  versus octahedral normal strain  $\epsilon_o$ . Since  $\sigma_o = 1/3\sigma_{ij}$  and  $\epsilon_o = 1/3\epsilon_{ij}$ , the mean stress (pressure)  $\sigma$  is synonymous with  $\sigma_o$ , and the volumetric strain  $\epsilon$  is equal to  $3\epsilon_o$ .

Based on the curves given in Figure 7, and in agreement with Stankowski and Gerstle,<sup>(18)</sup> the bulk modulus K was assigned the value

$$K = 2.1 \times 10^3 \text{ ksi} \quad (4.1)$$

Using the solid curve in Figure 7, together with the expression

$$\epsilon^P = \epsilon - \frac{\sigma}{K} \quad , \quad (4.2)$$

and the value of K given by Eq. (4.10), a curve of  $\sigma$  versus  $\epsilon^P$  was obtained which is shown in Figure 8. From the straight line portion of this figure, one finds by recalling Eq. (3.18) given earlier that

$$\begin{aligned} \beta &= 64.8 \\ \sigma_o &= 5 \text{ ksi} \end{aligned} \quad (4.3)$$

Using these values of  $\beta$  and  $\sigma_0$ , a plot was made of  $\sigma_0 - \sigma^*$  versus  $z_H$ , using the curve from Figure 8, and the definitions of  $\sigma^*$  and  $z_H$  given earlier by Eqs. (3.11) and (3.16), respectively. Six points, at equally spaced values of  $z_H$ , were chosen from this plot, and a two-term series of decaying exponentials of the form

$$\sigma_0 - \sigma^* = \sum_{r=1}^2 C_r e^{-\beta_r z_H} \quad (4.4)$$

was fit to these points by Prony's method. This led to the following values of  $C_r$  and  $\beta_r$ :

$$\begin{aligned} C_1 &= 2.434 \text{ ksi} & , & & \beta_1 &= 635 \\ C_2 &= 2.566 \text{ ksi} & , & & \beta_2 &= 2,289 \end{aligned} \quad (4.5)$$

A plot of Eq. (4.4), based on the constants given by Eq. (4.5), is shown in Figure 9, where the six points to which Eq. (4.4) was fit are also shown.

By comparing Eqs. (4.4) and (3.19), it then follows that

$$\begin{aligned} C_r &= \frac{K_r}{\beta + \lambda_r} \\ \beta_r &= \beta + \lambda_r \end{aligned} \quad (4.6)$$

from which we find

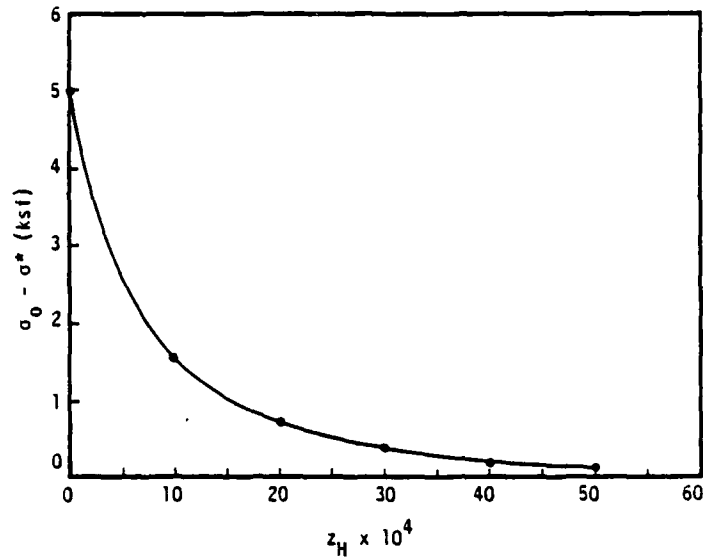


Figure 9. Representation of the  $\sigma_0 - \sigma^*$  versus  $z_H$  relationship by a two-term series of decaying exponentials. The solid circles are the equally-spaced points to which the series was fit.

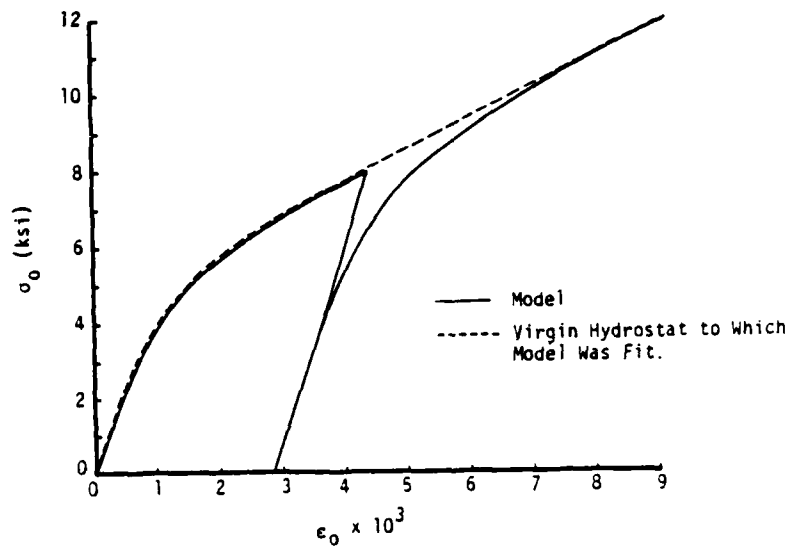


Figure 10. Octahedral normal stress versus octahedral normal strain for pure hydrostatic compression, including unloading and reloading.

$$\begin{aligned}
 K_1 &= 1.55 \times 10^3 \text{ ksi}, \lambda_1 = 570 \\
 K_2 &= 5.87 \times 10^3 \text{ ksi}, \lambda_2 = 2,224
 \end{aligned}
 \tag{4.7}$$

since  $\beta$  is known for Eq. (4.3). Therefore, Eq. (3.14), with the above values of the constants, completely defines the hydrostatic behavior of the model. An example of the hydrostatic behavior predicted by this model, including unloading and reloading response, is given in Figure 10. Comparison of this figure with the solid curve in Figure 7 shows that the model portrays the hydrostatic behavior quite well.

#### 4.1.2 Shear Parameters.

As noted earlier in Section 3.2, the most convenient and direct way of determining the shear parameters is from data on shear response under zero hydrostatic pressure. Unfortunately, Scavuzzo, *et al.*<sup>(17)</sup> did not investigate this case in their extensive study. They did, however, investigate shear behavior under several different fixed hydrostatic pressures in Tests 4-9 to 4-11; the resulting data will be used to determine the shear parameters and the shear-volumetric coupling parameters in this section.

A composite of the results for those portions of Tests 4-9 to 4-11 which consisted of shear at constant hydrostatic pressure is given in Figure 11. An inspection of this figure reveals some apparent discrepancies in the data. From the general characteristics of plain concrete reported in the literature, the initial slope at the onset of shear generally increases with confining pressure, and the shear stress-shear strain curves can be expected to fall above each other --

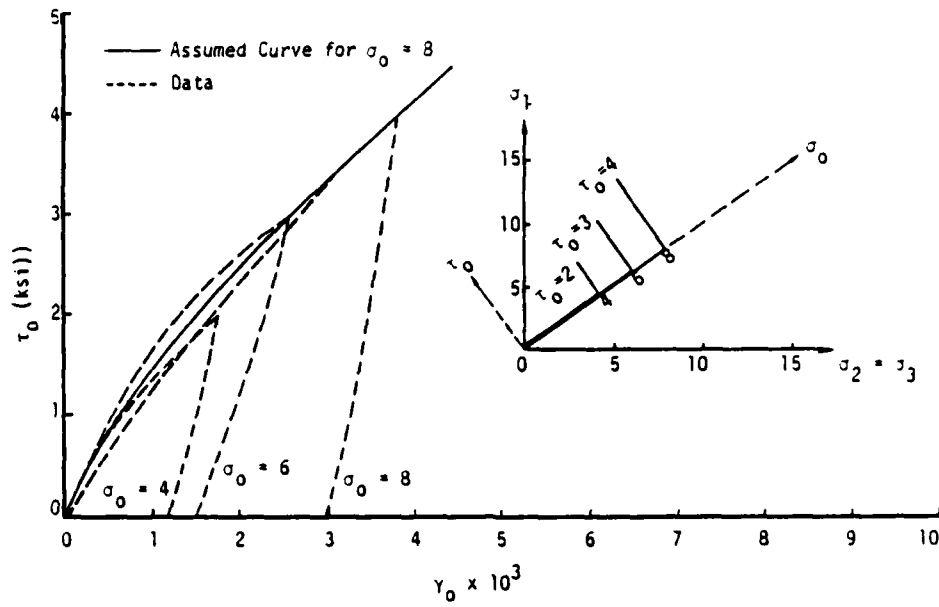


Figure 11. Octahedral shear stress versus octahedral shear strain for Tests 4-9 to 4-11.

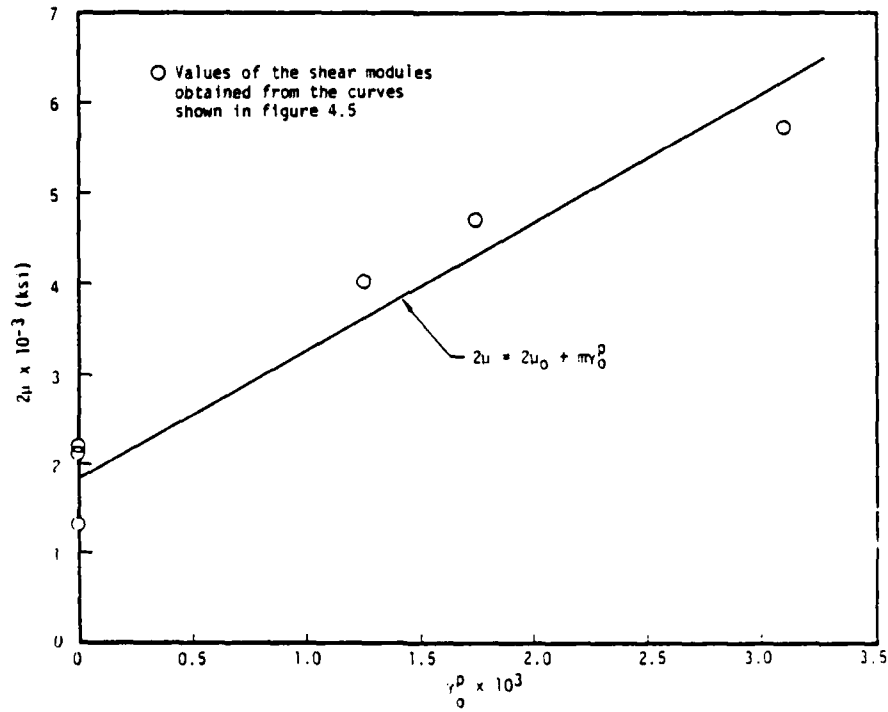


Figure 12. Dependence of shear modulus on octahedral shear stress.

not intersect -- as the confining pressure increases. Tests 4-9 and 4-10 follow the expected pattern, but Test 4-11, despite being at the highest confining pressure (8 ksi), does not; it has the smallest initial slope and exhibits softer response than Test 4-10. There is undoubtedly scatter in these data but since the tests were not repeated, the magnitude of the data scatter is unknown.

In Section 3.2, an approach for determining the shear parameters from shear data at constant hydrostatic pressures was described, which required the use of shear data obtained at fixed hydrostatic pressures that lay on the linear portion of the hydrostat. While the test conditions for Test 4-11 meet this requirement, i.e., shear at  $\sigma_0 = 8$  ksi, the data are somewhat suspect, as noted above. In view of this, we used our best judgement to construct a curve which we felt provided a more realistic description of the response of plain concrete to shear at  $\sigma_0 = 8$  ksi, and this curve is shown by the solid line in Figure 11. The reference pressure  $\sigma_R$  was therefore set at 8 ksi, and the shear parameters determined from the solid curve in Figure 11.

The shear modulus,  $2\mu$ , and its variation with deformation was also determined directly from the curves shown in Figure 11. The shear moduli were obtained from the initial slopes of the loading curves, as well as from the slopes of the initial portions of the unloading curves. Attempts were made to correlate the resulting values of  $2\mu$  against the plastic volumetric strain, the total volumetric strain, the octahedral shear strain and the plastic octahedral shear strain. The total volumetric strain and the plastic volumetric strain provided poor correlation, while the octahedral shear strain and the plastic octahedral shear strain led to reasonably good correlations. Adopting the plastic octahedral shear strain, a linear fit to the data points in Figure 12 led to the following expression for  $2\mu$ :

$$2\mu = 2\mu_0 + m \gamma_0^p \quad (4.8)$$

in which  $2\mu_0 = 1.83 \times 10^3$  ksi and  $m = 1.42 \times 10^6$  ksi.

By using Eq. (4.8), the following incremental expression for the plastic octahedral shear strain  $\gamma_0^p$

$$d\gamma_0^p = d\gamma_0 - \frac{d\tau_0}{2\mu}, \quad (4.9)$$

and the solid curve in Figure 11, the dependence of  $\tau_0$  on  $\gamma_0^p$  at the reference pressure  $\sigma_R = 8$  ksi was determined, and the result is depicted in Figure 13.

At this point, it becomes necessary to determine the shear-volumetric coupling coefficient  $k$  and, for this purpose, we consider Figure 14, which shows the manner in which the octahedral normal strain  $\epsilon_0$  varies with the octahedral shear stress  $\tau_0$  during shear at several different constant hydrostatic pressures. In the absence of contrary information, it will be assumed that volumetric changes which take place during shear at constant pressure are completely irreversible. On this basis, and using the results for  $\sigma_0 = 8$  ksi depicted in Figures 13 and 14, a plot of the plastic volumetric strain  $\epsilon^p$  versus the plastic octahedral shear strain  $\gamma_0^p$  was generated, and this is shown in Figure 15.

The model provides a theoretical expression for the dependence of  $\epsilon^p$  on  $\gamma_0^p$  through Eq. (3.43), given earlier, if we note that

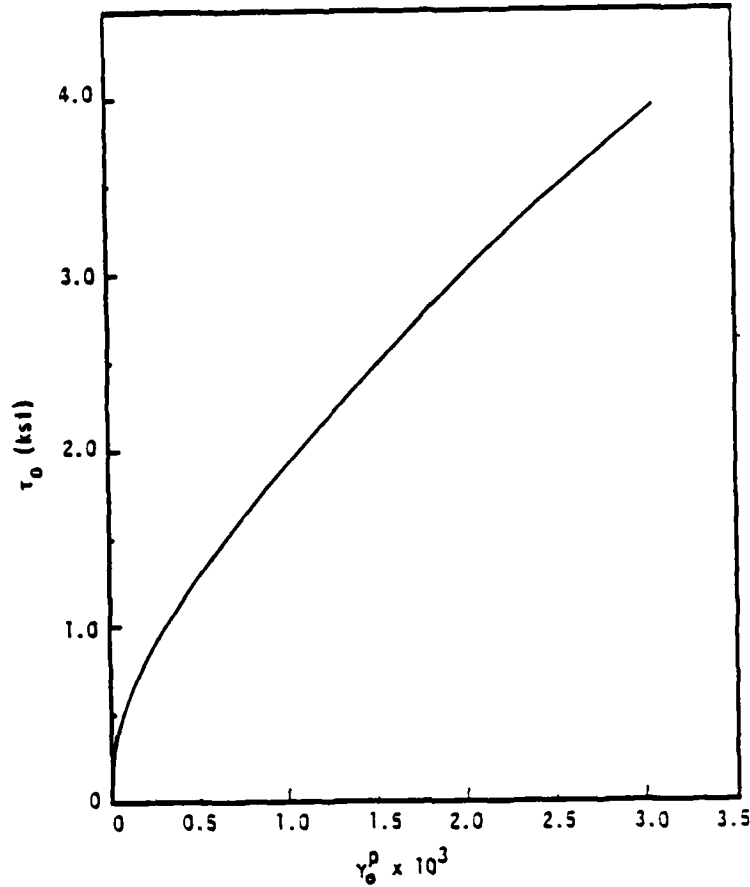


Figure 13. Dependence of the octahedral shear stress  $\tau_o$  on the plastic octahedral shear strain for a fixed hydrostatic pressure of 8 ksi.

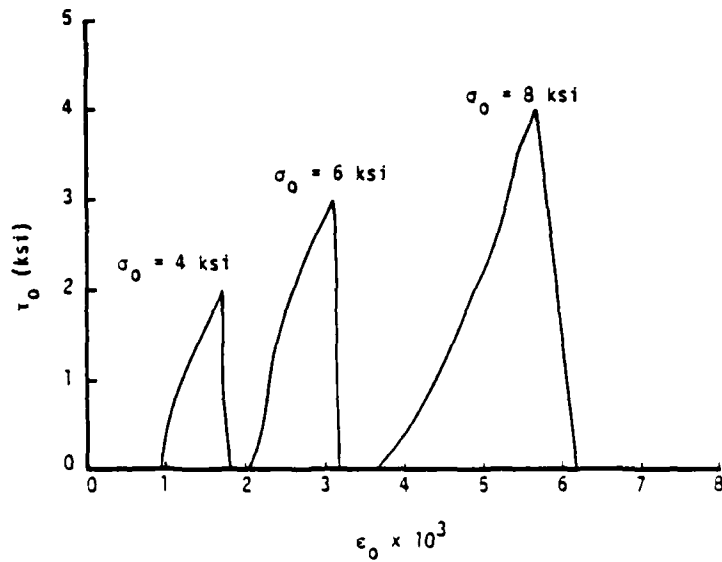


Figure 14. Dependence of the octahedral normal strain  $\epsilon_o$  on the octahedral shear stress  $\tau_o$  for several different values of constant hydrostatic pressure. Data are from Tests 4-9 to 4-11.

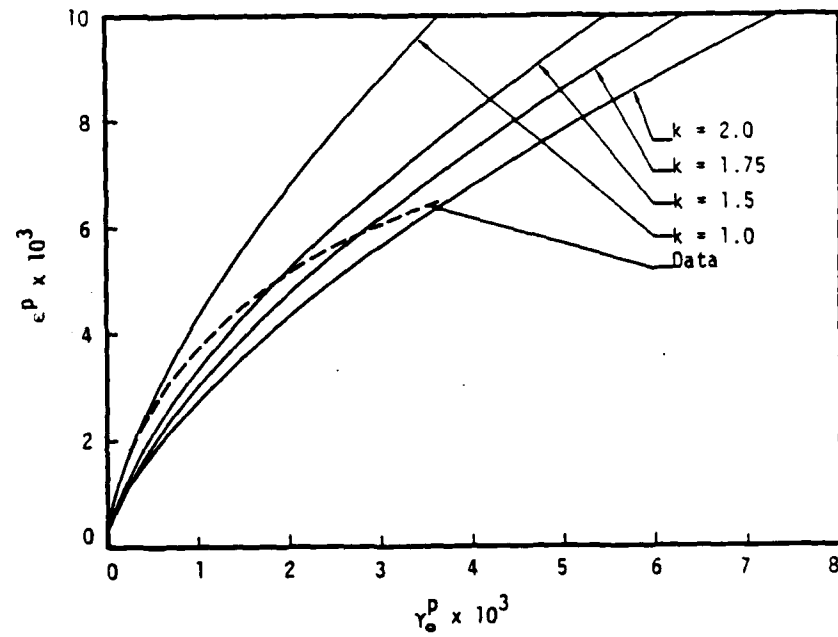


Figure 15. Shear-volumetric coupling at a constant hydrostatic pressure of 8 ksi. Data are from Test 4-11 in Reference 17.

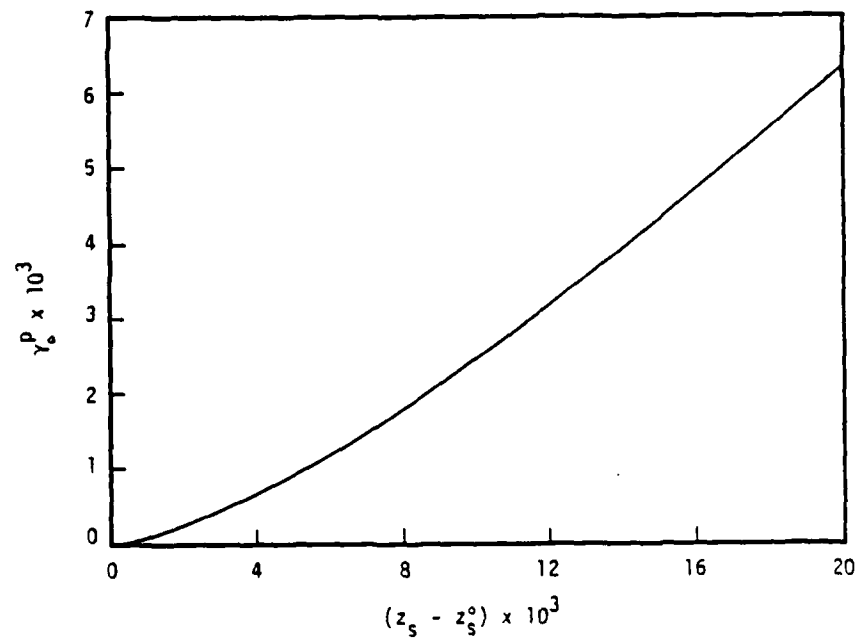


Figure 16. Dependence of  $\gamma_o^p$  on  $z_s - z_s^o$  predicted by Eqs. (4.12) and (4.13) for shear at a constant pressure of 8 ksi.

$$\gamma_0^P = \frac{1}{\sqrt{3}} \zeta_s \quad (4.10)$$

$$\epsilon^P = (x - 1)/(ak)$$

With these identifications, the dependence of  $\epsilon^P$  on  $\gamma_0^P$  is obtained for a specified value of  $k$ , since the constant  $a$  is known in terms of  $k$  through Eq. (3.42). In this manner, plots of  $\epsilon^P$  versus  $\gamma_0^P$  were generated with the aid of Eq. (3.43) for a range of assumed values for  $k$ , and the results are shown in Figure 15. From an inspection of this figure, the curve corresponding to  $k = 1.5$  appears to provide the best overall description of the data; thus, we set

$$k = 1.5 \quad (4.11)$$

in the model.

In Appendix C, the following expression is derived, relating  $\zeta_s$  and  $z_s$  during shear at constant pressure, for the case in which  $\sigma$  is at the reference pressure  $\sigma_R$  and on the linear portion of the virgin hydrostat:

$$\zeta_s = \frac{1}{2a} \left\{ \sqrt{2a z_s} \sqrt{1 + 2a z_s} - \log \left| \sqrt{2a z_s} - \sqrt{1 + 2a z_s} \right| \right\} \quad (4.12)$$

During shear at constant pressure, it can be shown that

$$\zeta_s = \sqrt{3} \gamma_0^P \quad (4.13)$$

which, when combined with Eq. (4.12), provides a relationship between  $\gamma_0^p$  and  $z_s$  during shear at constant pressure for a prescribed value of  $a$ . Adopting the value of  $k$  given in Eq. (4.11), the value of the constant  $a$  is then known, and the resulting expression given by Eqs. (4.12) and (4.13) between  $\gamma_0^p$  and  $z_s$  is as shown in Figure 16. Using this result, and the relationship between  $\tau_0$  and  $\gamma_0^p$  given in Figure 13, the dependence of  $\tau_0$  on  $z_s$  during shear at constant pressure can be constructed. The numerical method described in Section 3.2 may now be utilized in conjunction with the  $\tau_0$  versus  $z_s$  relationship just found to give  $M(z_s)$ , where  $M$  is defined by Eq. (3.64). In this manner, the result shown in Figure 17 was obtained. Using this in conjunction with Eq. (3.69), the shear kernel function  $\rho(z_s)$  can be found by differentiation of the  $M(z_s)$  relationship. A two-term series of decay exponentials of the form

$$\rho(z_s) = \sum_{r=1}^2 A_r e^{-a_r z_s} \quad (4.14)$$

was fit to the shear kernel by Prony's method; this led to the following values for the  $A_r$  and  $a_r$ .\*

$$\begin{aligned} A_1 &= 1.46 \times 10^3 \text{ ksi} \quad , \quad a_1 = 100 \\ A_2 &= 19.0 \times 10^3 \text{ ksi} \quad , \quad a_2 = 6,554. \end{aligned} \quad (4.15)$$

---

\*. Because the numerical inversion of Eq. (3.53) was only approximate (see Figure 17), the  $\rho(z)$  so obtained was also approximate. As a result, an adjustment in the value of  $a$ , to that listed in Eq. (4.15) was made to provide a better description of the shear behavior.

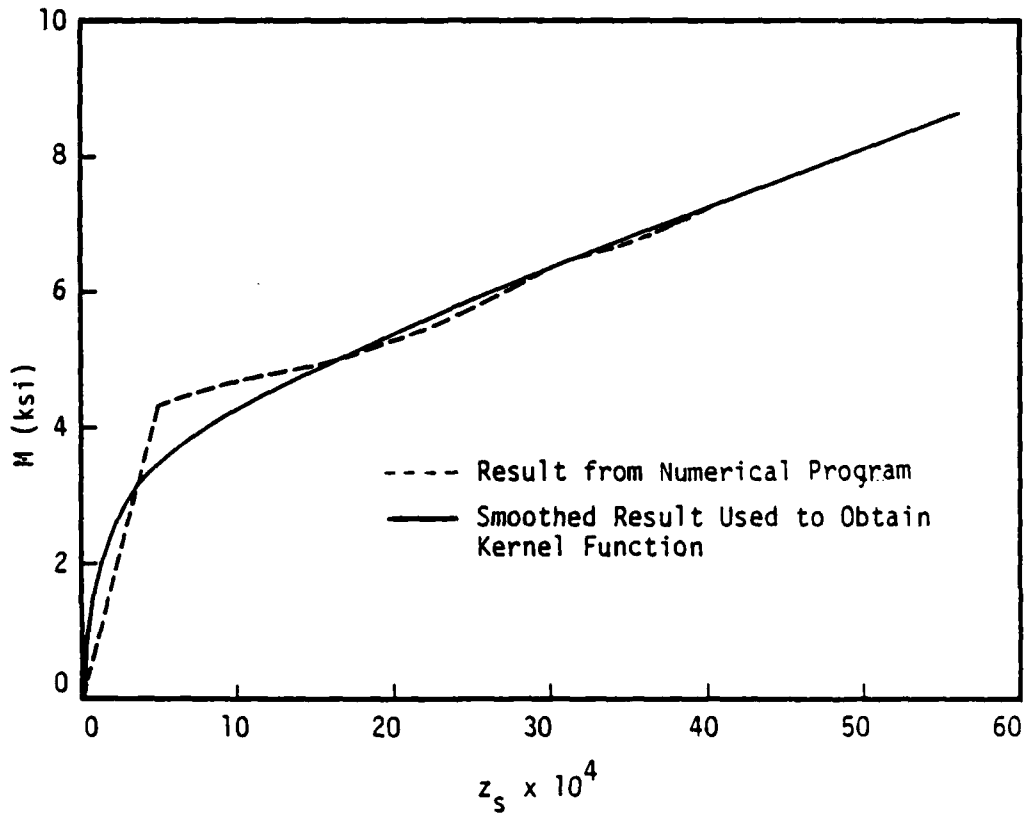


Figure 17. Dependence of M on  $z_s$  for shear at a fixed hydrostatic pressure of 8 ksi.

Finally, on the basis of the failure data given by Stankowski,<sup>(30)</sup> the following expression for the function  $F_s$  was adopted for use in the present study:

$$F_s = \frac{\tau^* + \beta_s \sigma}{\tau^* + \beta_s \sigma_R} \quad (4.16a)$$

in which

$$\tau^* = 2 \text{ ksi}$$

$$\beta_s = 0.5 \quad (4.16b)$$

$$\sigma_R = 8 \text{ ksi}$$

This completes the specification of the endochronic concrete model.

#### 4.2 INTERNAL CONSISTENCY OF MODEL, DATA AND FITTING PROCEDURE.

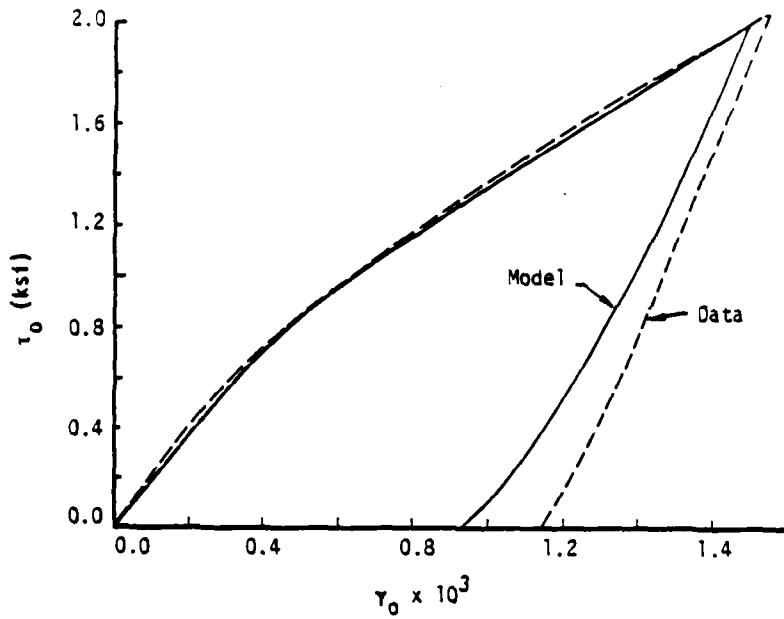
We return now to determine how well the plain concrete model just specified can describe the data to which it was fit, namely, the data from Tests 4-9 to 4-11 of Reference 17.\* Such an exercise does not, of course, constitute a proof-test of the model, but simply provides a test of the internal consistency of the fitting procedure. It should be remembered that plain concrete data exhibits significant data scatter and, in comparing a model prediction against an indivi-

---

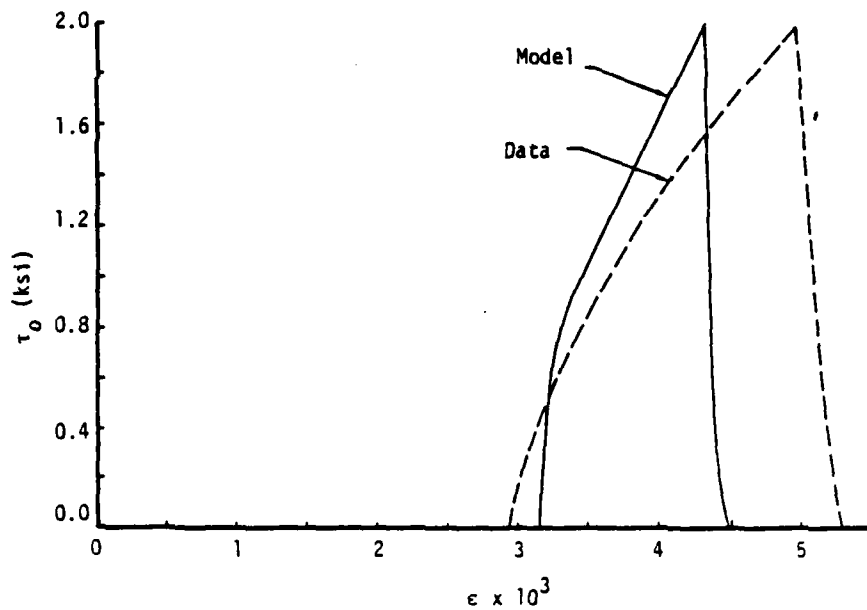
\*. A comparison between the measured and predicted hydrostatic behavior was given earlier in Figure 15, and will not be repeated here.

dual test result, one cannot expect to obtain the same level of agreement as is found for example in metals. With plain concrete, one is looking more for a model that captures the overall, general characteristics of response.

To explore the ability of the model to describe the data from Tests 4-9 to 4-11, the model was driven around the appropriate prescribed stress paths for these tests, using a stress-driven computer program based upon the explicit incremental numerical scheme described in Appendix B. The results from these calculations are depicted in Figures 18 to 20. As an inspection of these figures reveals, the overall agreement between predictions and the data is quite good, considering the uncertainty in the data discussed earlier. The figures reveal that the main discrepancies lie in the unloading behavior, with the model showing noticeably more curvature of the unloading path -- and hence more hysteresis -- than the data. Although no effort was made in the present study to refine the model so that it would more closely describe the unloading behavior, such an improvement is straightforward and will be accomplished in a future study.

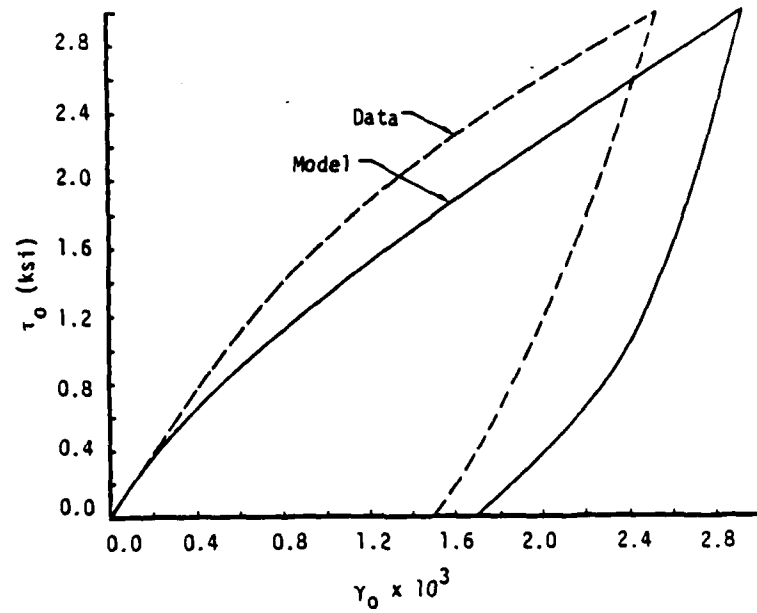


(a) Octahedral shear stress versus octahedral shear strain.

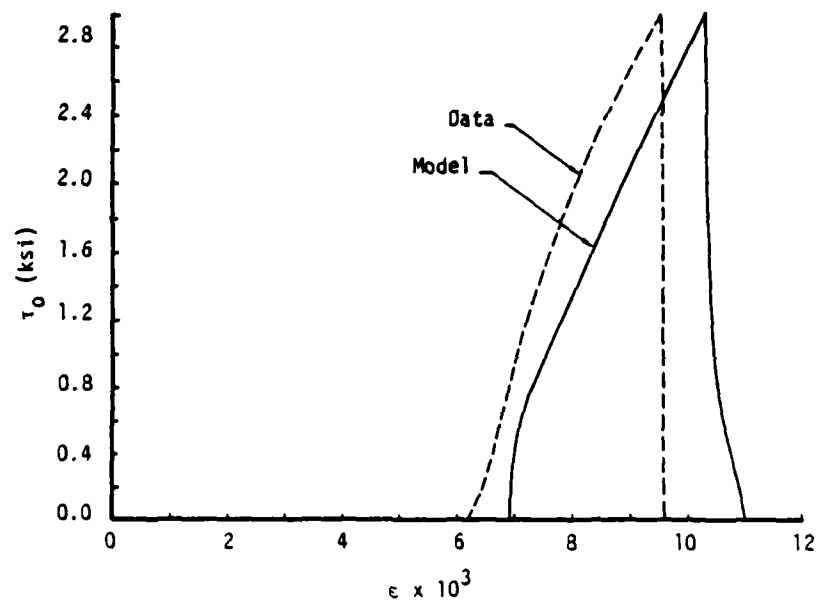


(b) Octrahedral shear stress versus volumetric strain.

Figure 18. Measured and predicted responses to shear at a fixed hydrostatic pressure of 4 ksi (Test 4-9).

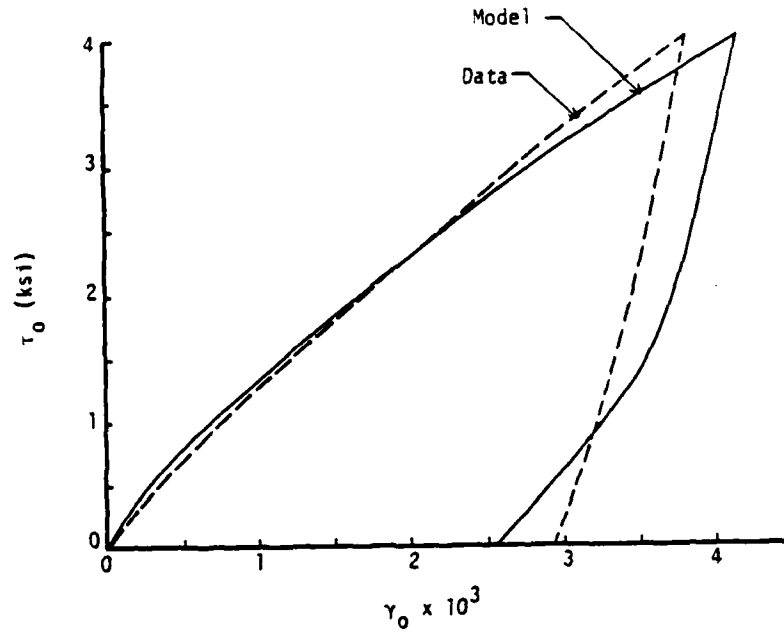


(a) Octahedral shear stress versus octahedral shear strain.

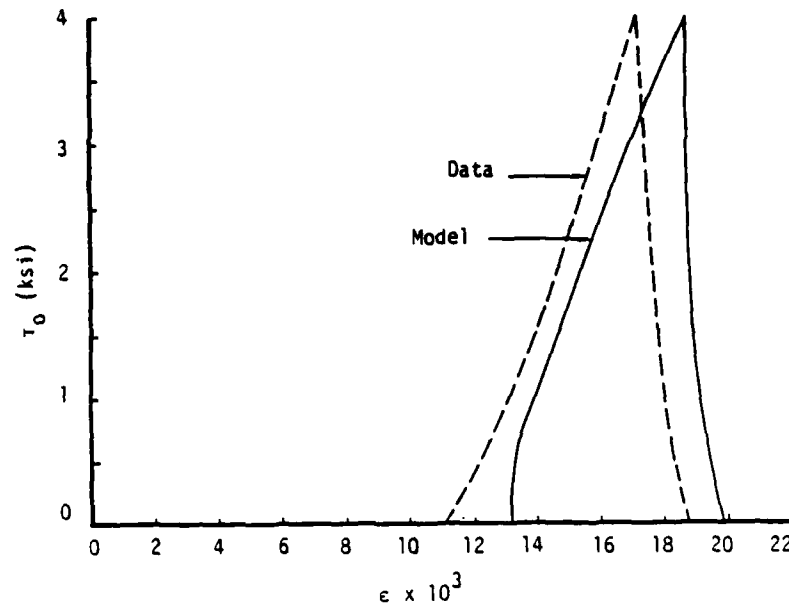


(b) Octahedral shear stress versus volumetric strain.

Figure 19. Measured and predicted responses to shear at a fixed hydrostatic pressure of 6 ksi. (Test 4-10).



(a) Octahedral shear stress versus octahedral shear strain.



(b) Octahedral shear stress versus volumetric strain.

Figure 20. Measured and predicted responses to shear at a fixed hydrostatic pressure of 8 ksi (Test 4-11).

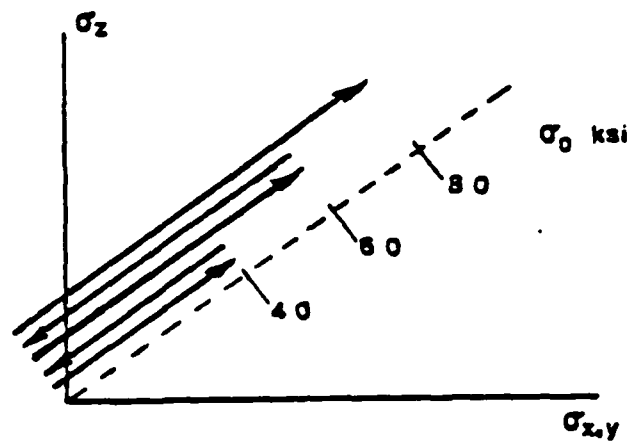
## SECTION 5

### PROOF-TESTS OF MODEL OVER COMPLEX STRESS PATHS

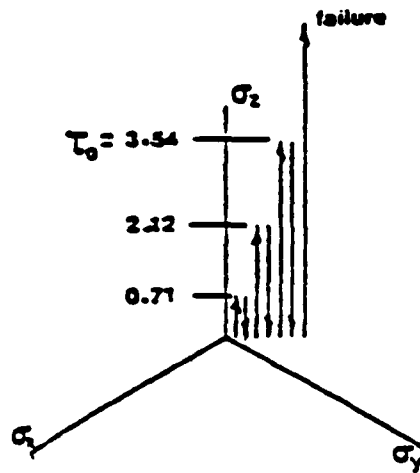
In the preceding section, the endochronic constitutive model developed in Section 3 was applied to the plain concrete data presented in Reference 17, with the model parameters evaluated from a small subset of the reported data. The ability of the resulting model to accurately portray the data to which it was fit was also described. The test program reported in Reference 17 consisted of six different series of stress-controlled tests, each series being designed to explore a particular facet of plain concrete behavior. In that which follows, the model is proof-tested by examining its capability to predict the measured response around a selected number of prescribed complex stress paths from this test series. None of the stress path tests considered in this section were used in fitting the model parameters, and no optimization techniques were employed to achieve the results presented below.

#### 5.1 SERIES NO. 1.

This test series was designed to explore the response of plain concrete to triaxial load cycles which do not exhibit stress reversals. Each test was repeated once. The model was applied in the present study to Test 1-1 from this series, for which the prescribed load paths are shown in Figure 21. The loading consisted first of cyclic hydrostatic loading up to 8 ksi, as shown in Figure 21(a), followed by cyclic deviatoric loading along the triaxial compression path, as illustrated in Figure 21(b). The predicted and measured response for this loading history are given in Figure 22. As this figure reveals, the predicted and measured responses are in good agreement, considering the data scatter which can be assessed by



(a) Cyclic hydrostatic loading.



(b) Cyclic deviatoric loading along the triaxial compression path.

Figure 21. Stress paths for Test 1-1.

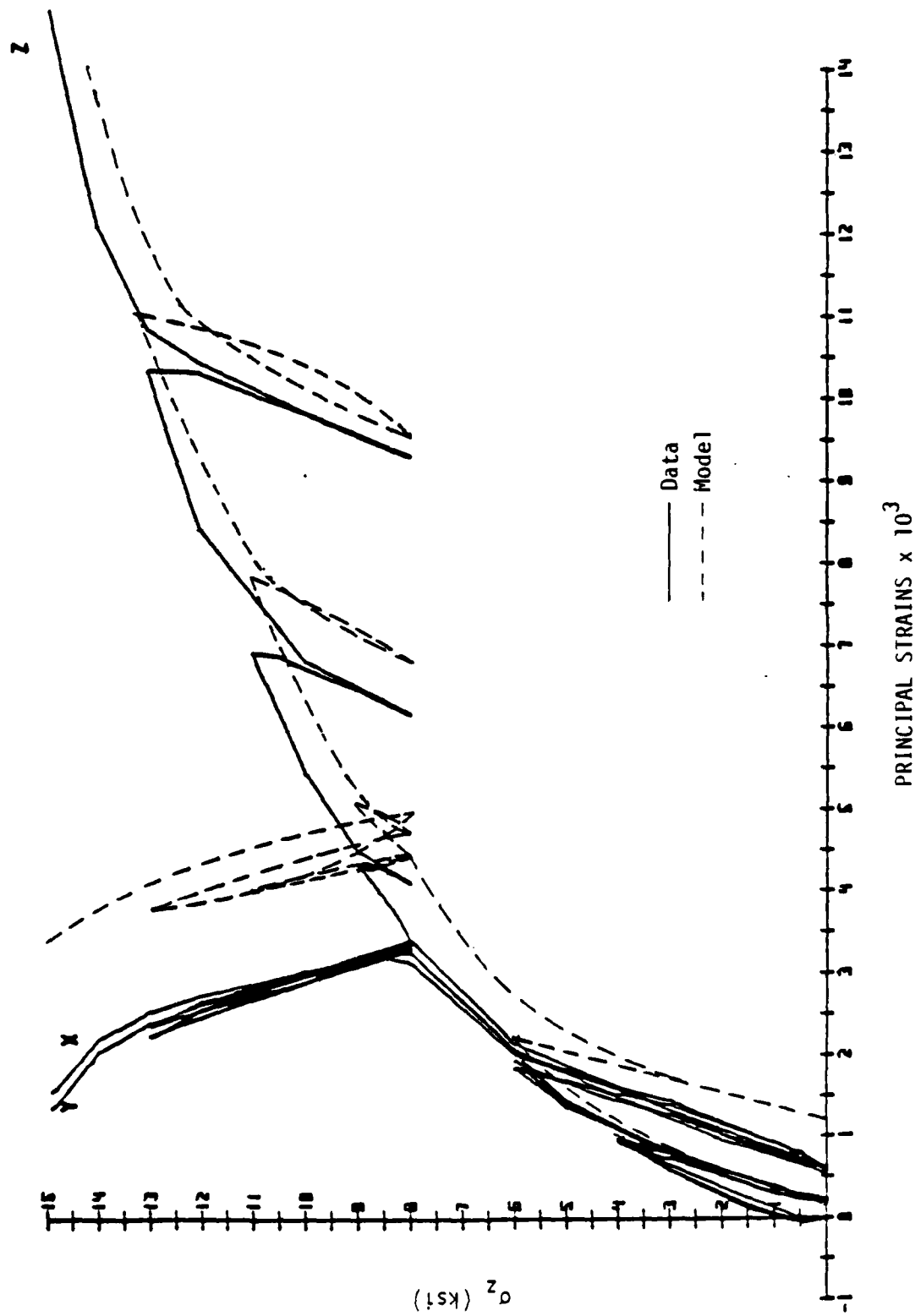


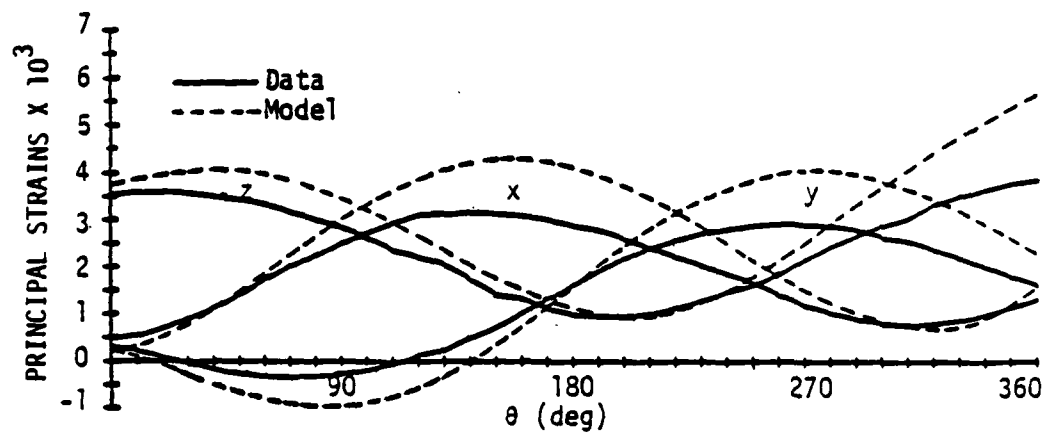
Figure 22. Predicted and measured response of plain concrete to Test 1-1.

comparing the results from Test 1-1 with those from the replicate test given in Reference 17, i.e., Test No. 1-10. If the data curve in Figure 22 was simply shifted to the right a small amount, the agreement would be excellent. Such a shift appears to be justified on the basis of the data scatter, since a comparison of the hydrostatic compression curves in Figures 7 and 22 reveals that the measured hydrostatic response in Figure 22 is stiffer than the data given in Figure 7 to which the model was fit. Aside from this difference, the qualitative features of the plain concrete behavior are obviously captured very well by the model.

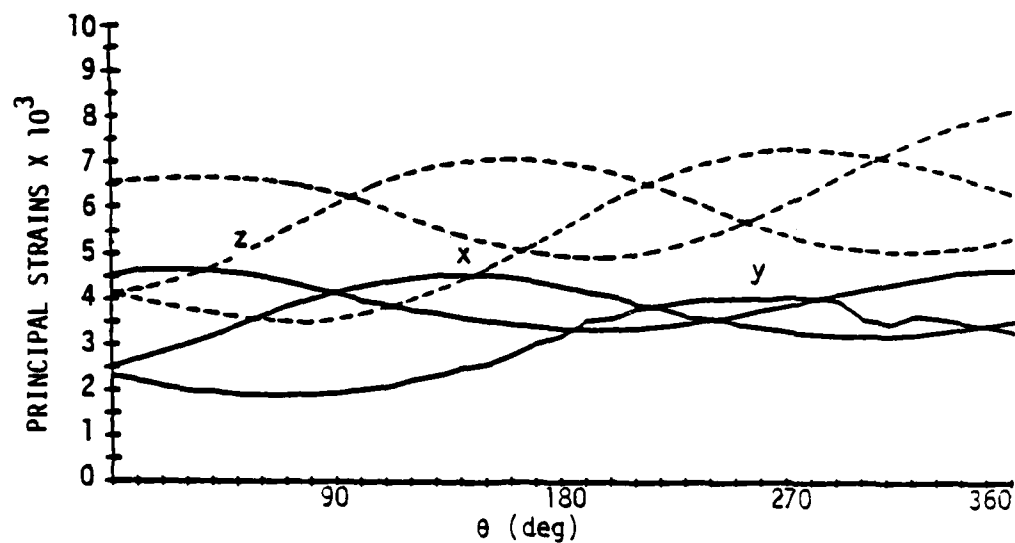
## 5.2 SERIES NO. 3.

Test Series No. 3 was designed to examine the behavior of plain concrete to circular stress paths in the deviatoric plane. The stress paths consisted of monotonic hydrostatic loading, then proportional deviatoric loading along the triaxial compression path, and finally a circular load path in the deviatoric plane. In the present study, the load paths corresponding to Tests 3-3 and 3-4, as well as Tests 3-10, 3-11 and 3-12 were considered; Tests 3-3 and 3-4 had the same load path, as was also the case for Tests 3-10 to 3-12.

Figure 23 gives the responses predicted by the model to the circular stressed paths, as well as the corresponding data. Again, the overall agreement between predictions and measurements is considered good for plain concrete. If the data curve in Figure 23(b) were translated vertically upward by a sufficient amount, the results would show very good agreement. However, such a translation does not appear to be justified if one considers the data from Tests 3-10 and 3-11, which had load paths identical to Test 3-12. Thus, the model appears to be too soft during the proportional deviatoric leg of Test 3-12.



(b) Test 3-3 in which  $\sigma_0 = 4$  ksi and  $\tau_0 = 2$  ksi.



(c) Test 3-12 in which  $\sigma_0 = 8$  ksi and  $\tau_0 = 1.5$  ksi.

Figure 23. Response of plain concrete to circular stress paths in the deviatoric plane.

The results shown in Figure 23 are also of interest from another point of view. Recently, the new endochronic theory -- which forms the basis of the model developed herein -- was criticized by Bazant, Krizek and Shieh<sup>(29)</sup> as being unable to correctly describe the response of geomaterials, such as concrete, to what has been termed "loading-to-the-side". Without providing supporting experimental evidence, they claim that the model is unrealistic because it predicts purely elastic response for infinitesimal loading-to-the-side. To the authors' knowledge, no data are currently available for plain concrete which define its response to loading-to-the-side. Moreover, while the models' response to infinitesimal loading-to-the-side is purely elastic, its response to finite loading-to-the-side is inelastic. In Tests 3-3 and 3-12, the plain concrete was subjected to loading-to-the-side, at least at the beginning of the circular stress path and possibly when the path crossed the other two principal stress axes. In view of the reasonably good agreement between the data and the predictions for these paths, the criticisms by Bazant, *et al.*<sup>(29)</sup> appear to be premature and unjustified. For further elaboration on this point, see the discussion by Read.<sup>(34)</sup>

### 5.3 SERIES NO. 4.

This series consisted of the largest number of tests, namely 22. In general, the tests were designed to explore several aspects of axisymmetric stress paths, i.e., paths for which at least two of the principal stresses were equal; this included (a) development of shear strain due to hydrostatic pressure increments in the presence of prior deviatoric stress, (b) dependence of response on stress path, and (c) behavior under nonproportional deviatoric stress paths. In that which follows, eight selected stress paths from Series No. 4 which

shed light on each of the above aspects of plain concrete behavior are considered.

Test 4-1 and its replicate, Test 4-2, provide insight into the development of shear strain during hydrostatic pressure increments in the presence of non-vanishing shear stress, i.e., shear-volumetric coupling. These tests followed the stress path described by the insert in Figure 24. This figure also shows the response to the prescribed stress path predicted by the present model, as well as the responses measured in the tests. The section of the path from (b) to (c) is of primary interest, since this is where the shear-volumetric coupling occurs under purely hydrostatic increments. As the results given in the figure indicate, the agreement between the model and the two sets of data is excellent.

Next, we consider Tests 4-9, 4-11, 4-13, 4-15, 4-16 and 4-17. This group of tests was designed to explore the effect, if any, of stress path dependence on plain concrete behavior. Except for Test 4-13, the remaining tests consist of stress paths that, while quite different from one another, nevertheless have at some point a common stress state, namely,  $\sigma_0 = 8$  ksi and  $\tau_0 = 4$  ksi. Thus, by comparing the strains measured at this stress state in the various tests allows an assessment of the magnitude of the stress path effect.

Table I summarizes the principal strains in the various tests that were measured in Reference 17 at the common stress state.

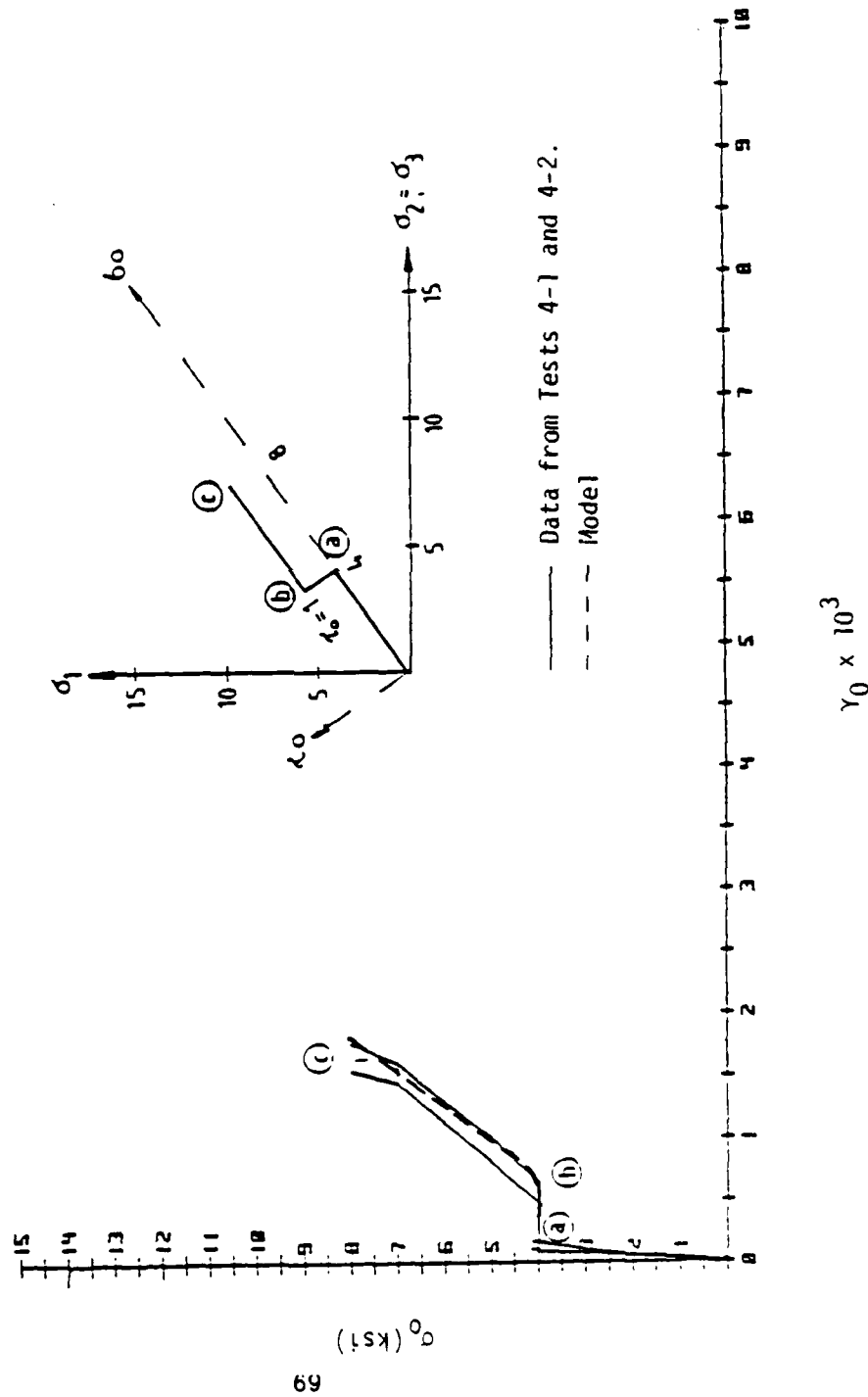


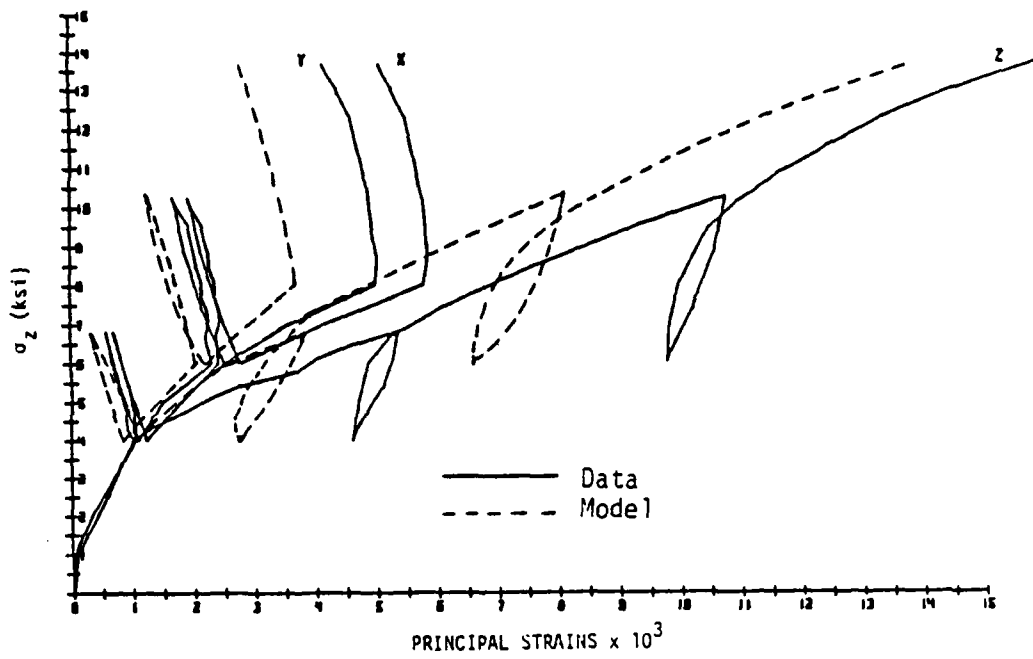
Figure 24. Dependence of pressure  $\sigma$  on octahedral shear strain  $\gamma_0$  for Tests 4-1 and 4-2.

Table 1. Summary of the Principal Strains Measured at the Common Stress State of  $\sigma_o = 8$  ksi and  $\tau_o = 4$  ksi.

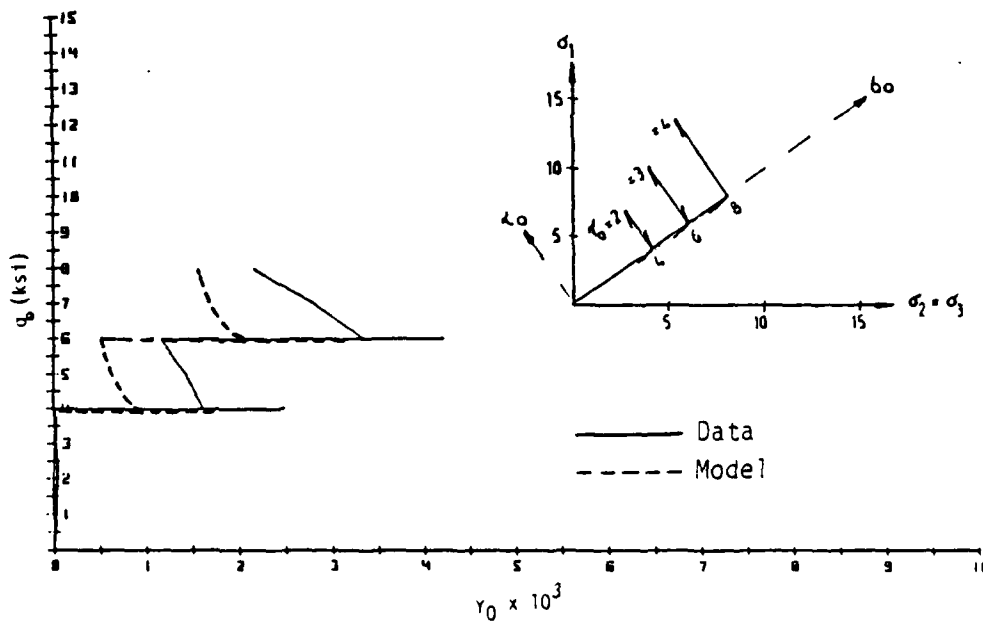
Test Number	Principal Strains $\times 10^3$		
	$\epsilon_x$	$\epsilon_y$	$\epsilon_z$
4-09	5.10	4.18	15.89
4-11	2.86	3.13	11.15
4-15	1.64	1.72	12.72
4-16	10.25	10.00	13.27
4-17	1.19	1.33	12.78

As an inspection of this table reveals, there is substantial dependence of the deformation at the common stress state on the particular path taken to get to that state. The major principal strain,  $\epsilon_z$ , varies from  $11.15 \times 10^{-3}$  to  $15.89 \times 10^{-3}$ , while the other two strains show much greater variation, ranging from about  $1 \times 10^{-3}$  to  $10 \times 10^{-3}$ .

The ability of the present model to describe the measured responses for Tests 4-9, 4-11, 4-13, 4-15, 4-16 and 4-17 is illustrated in Figures 25 to 32. Unfortunately, none of the tests in this group were repeated, so we have no insight into the level of data scatter. In view of the usual scatter found in concrete data, however, the agreement between the model predictions and the data is considered excellent; this agreement demonstrates the capability of the present model to account for the influence of the stress path on the resulting response.

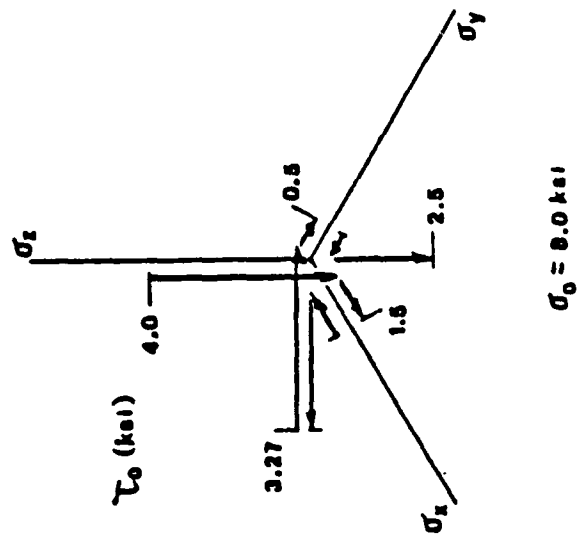


(a) Major principal stress versus principal strains.

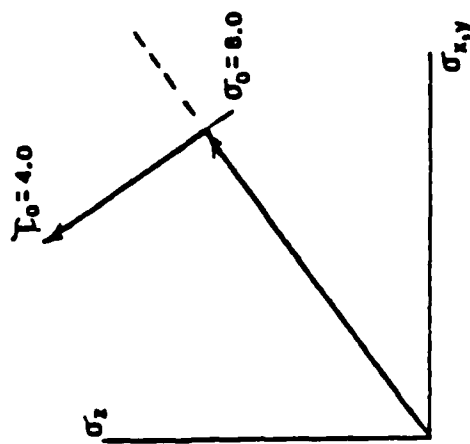


(b) Octahedral normal stress versus octahedral shear strain.

Figure 25. Measured and predicted responses for Test 4-9.

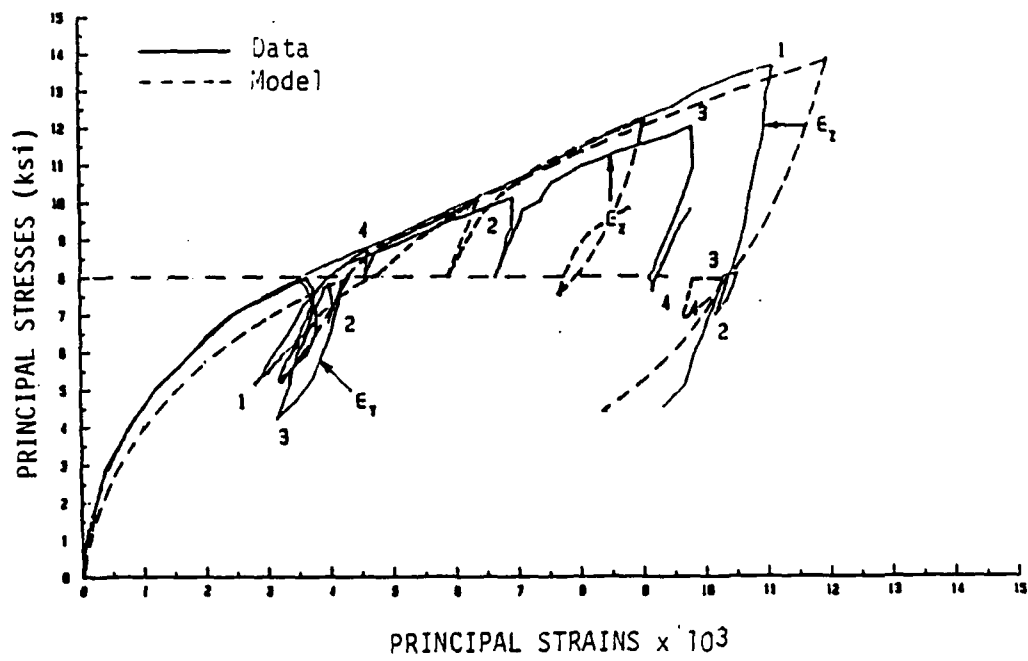


(b) Deviatoric plane.

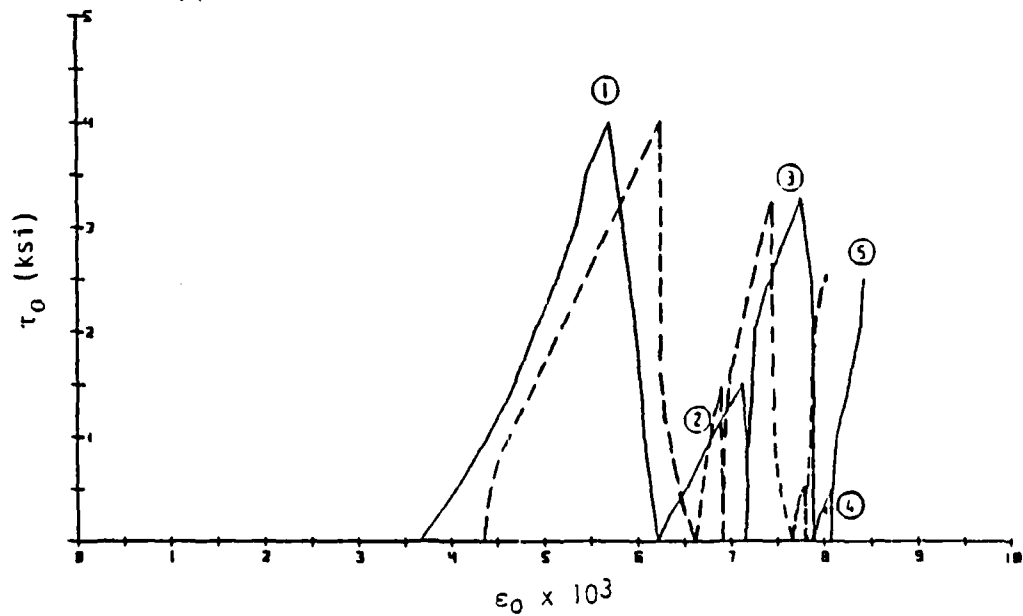


(a) Rendulic plane.

Figure 26. Stress path for Test 4-11.

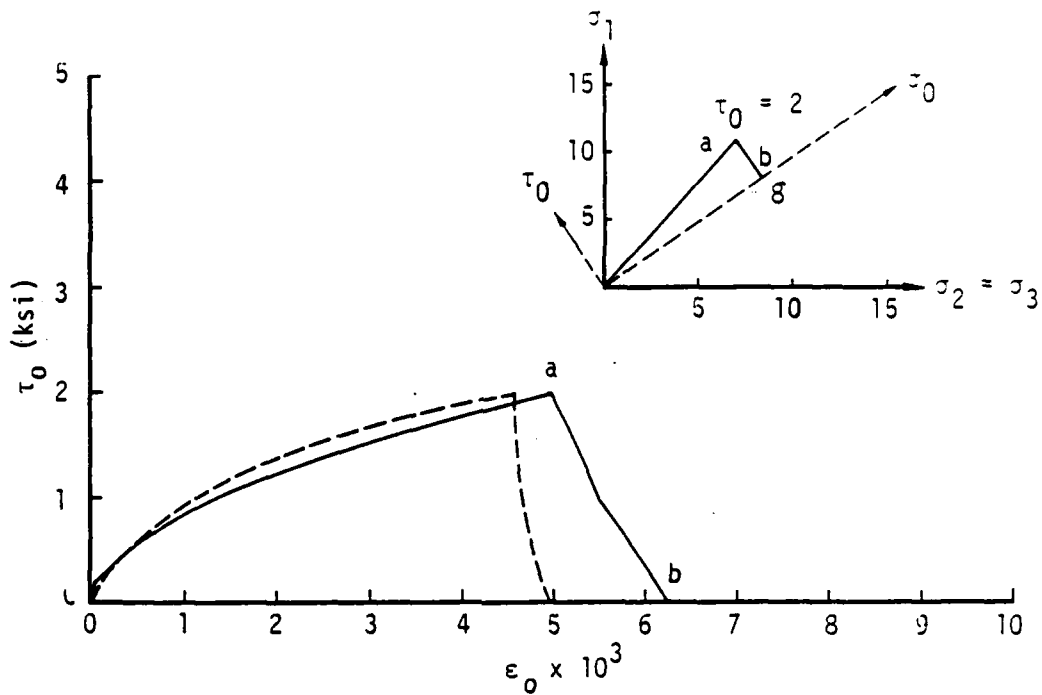


(a) Principal stresses versus principal strains.

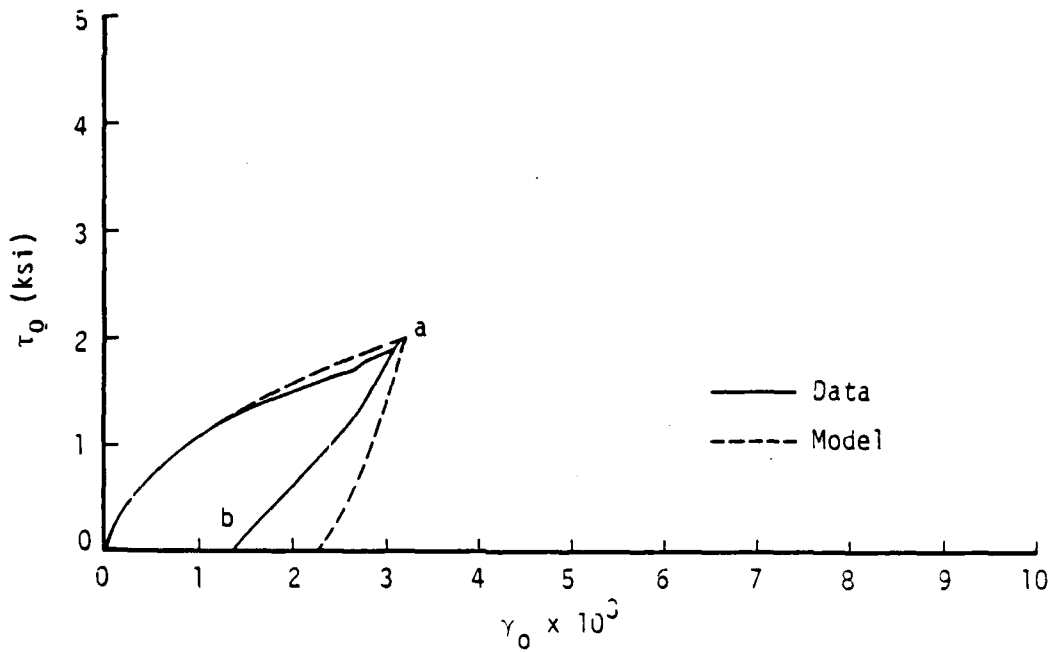


(b) Octahedral shear stress versus octahedral normal strain.

Figure 27. Measured and predicted responses for Test 4-11.

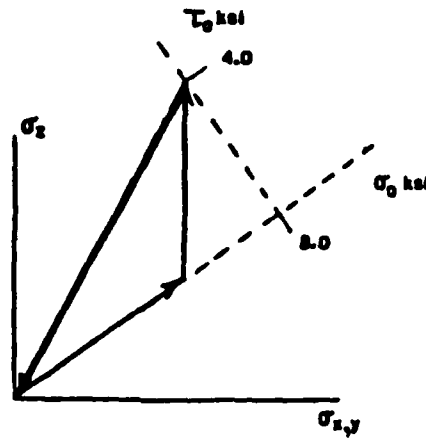


(a) Octahedral shear stress versus octahedral normal strain.

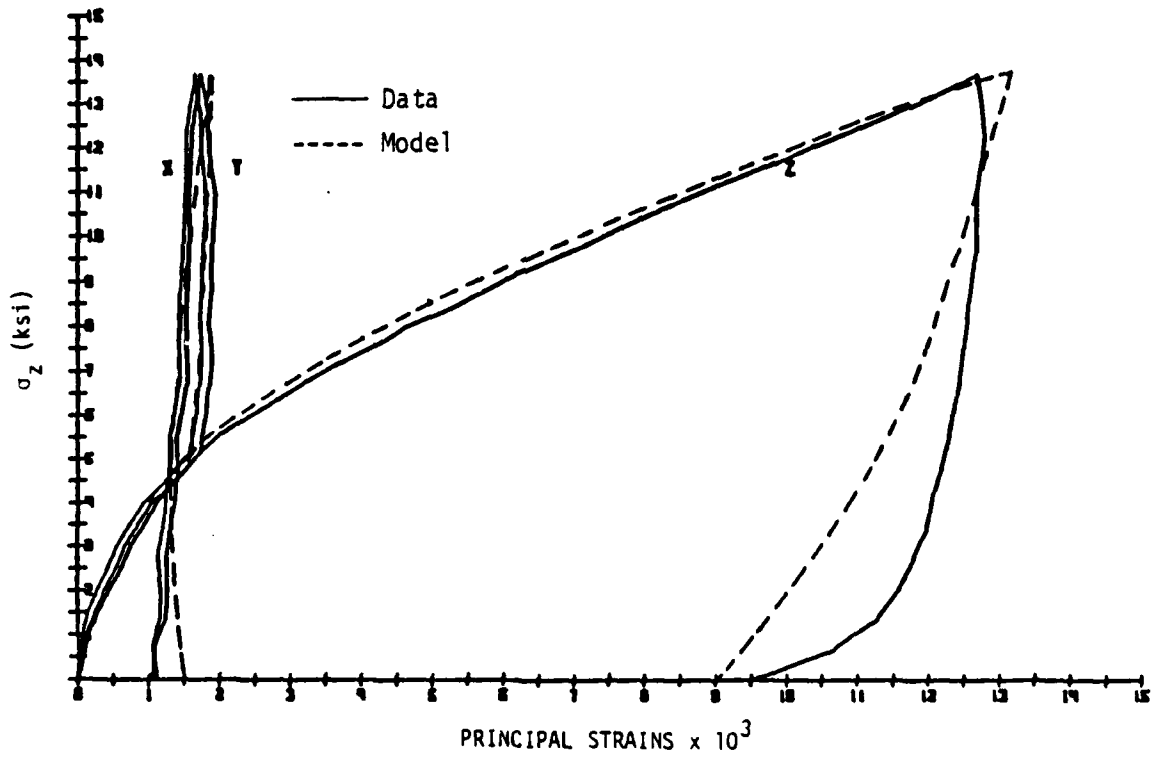


(b) Octahedral shear stress versus octahedral shear stress.

Figure 28. measured and predicted responses for Test 4-13.

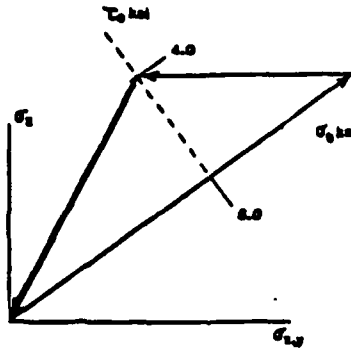


(a) Stress path.

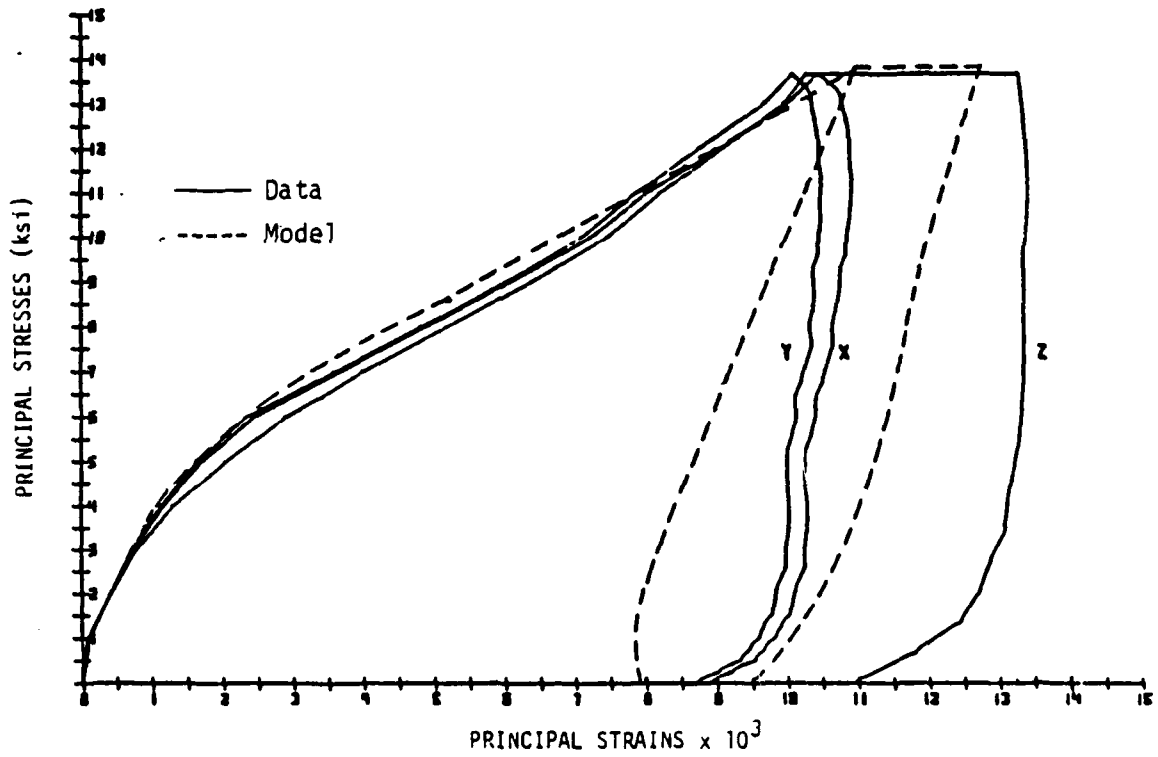


(b) Major principal stress versus principal strains.

Figure 29. Measured and predicted responses for Test 4-15.



(a) Stress path.



(b) Principal stresses versus principal strains for Test 4-16.

Figure 30. Measured and predicted responses for Test 4-16.

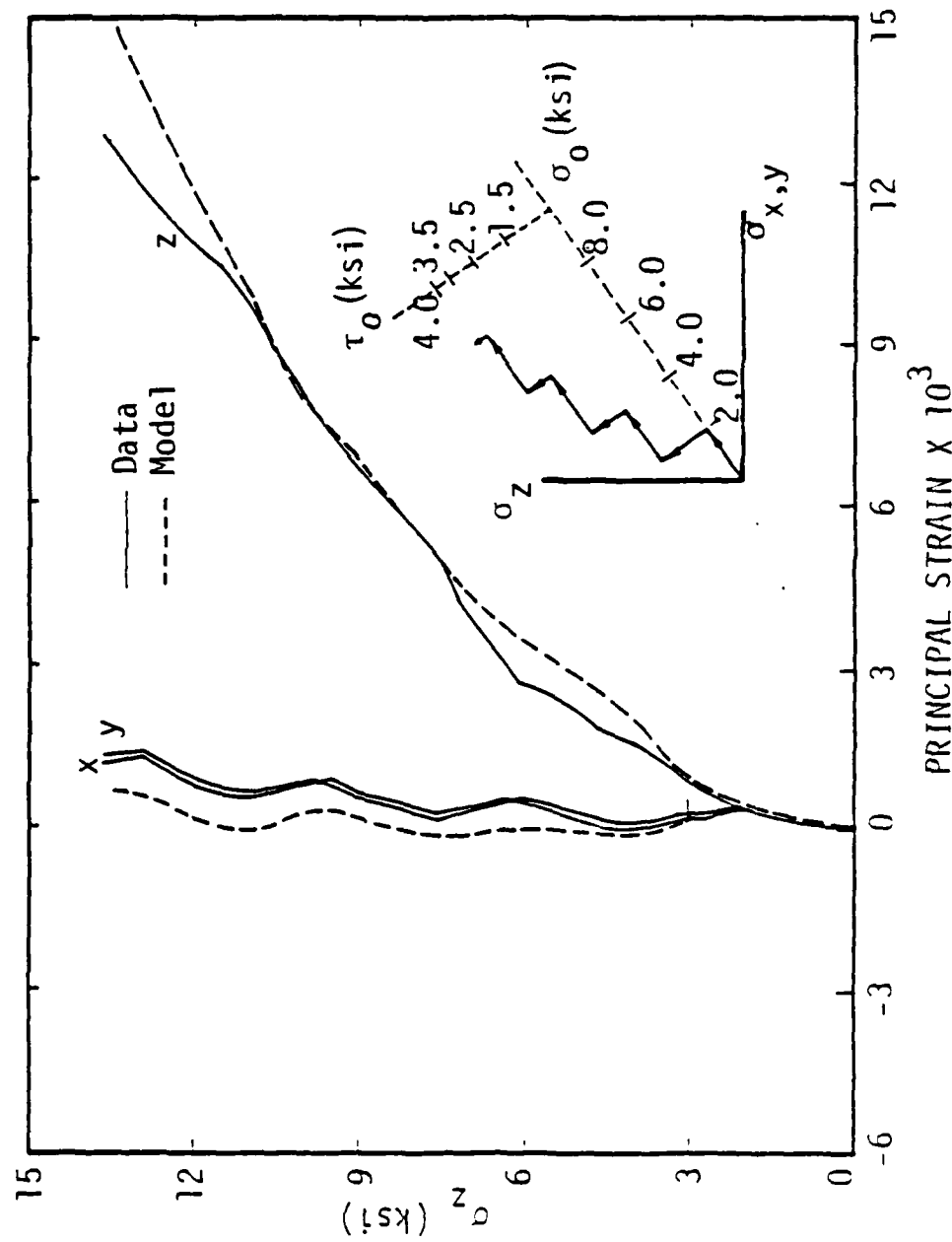
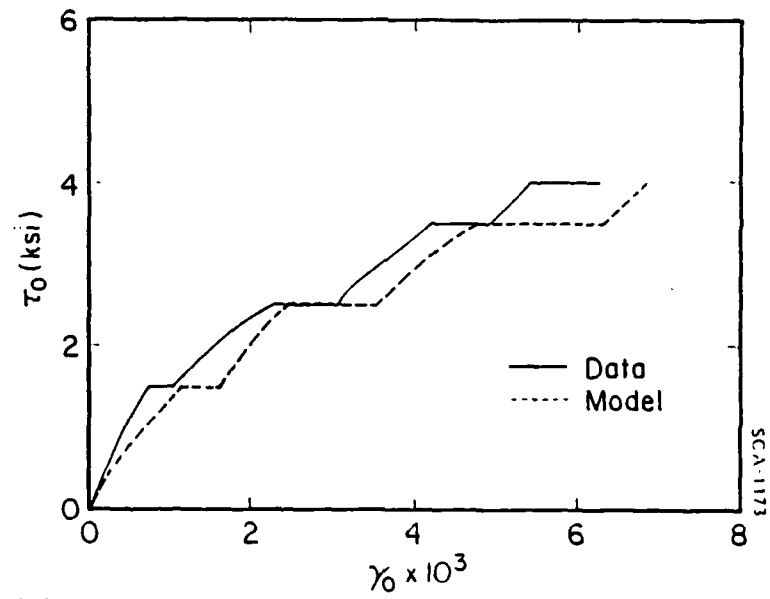
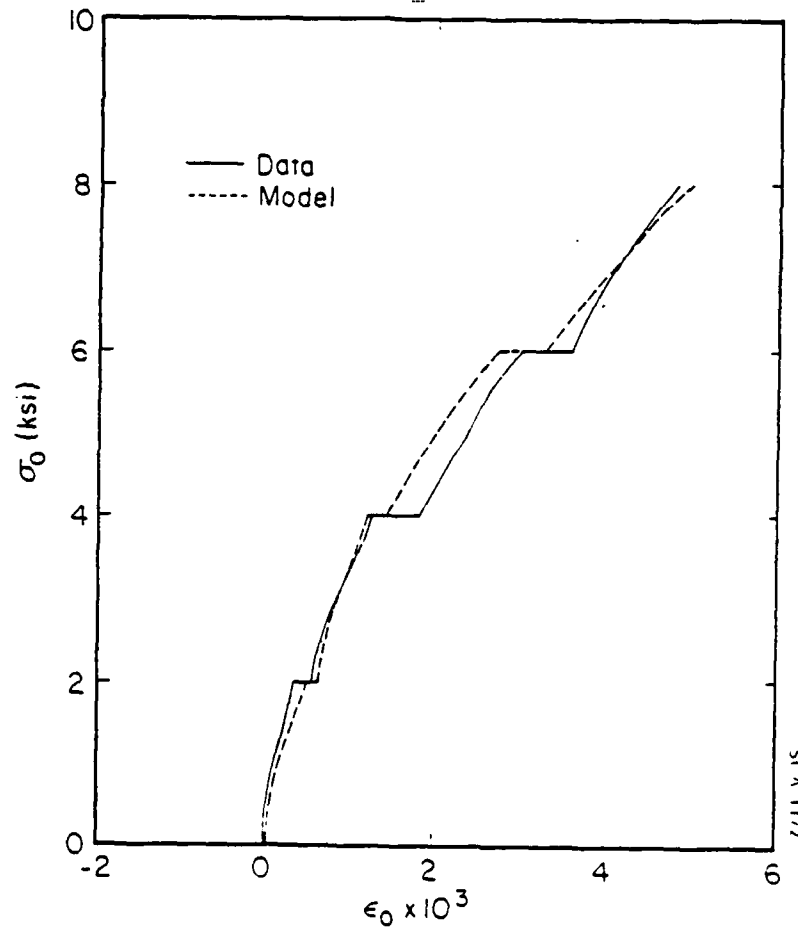


Figure 31. Major principal stress versus principal strains for Test 4-17.

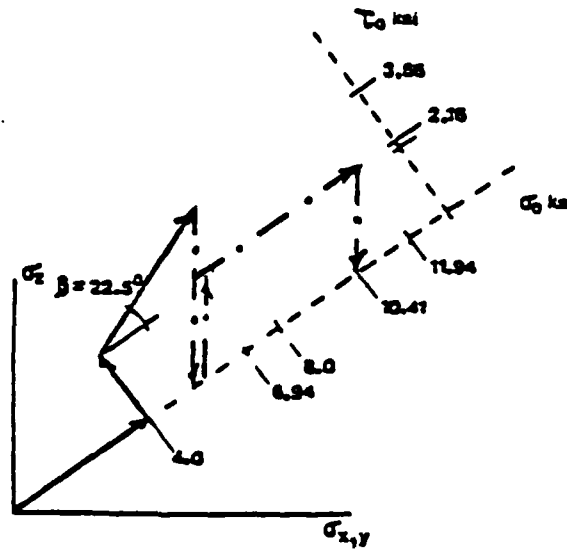


(a) Octahedral shear stress versus octahedral shear strain.

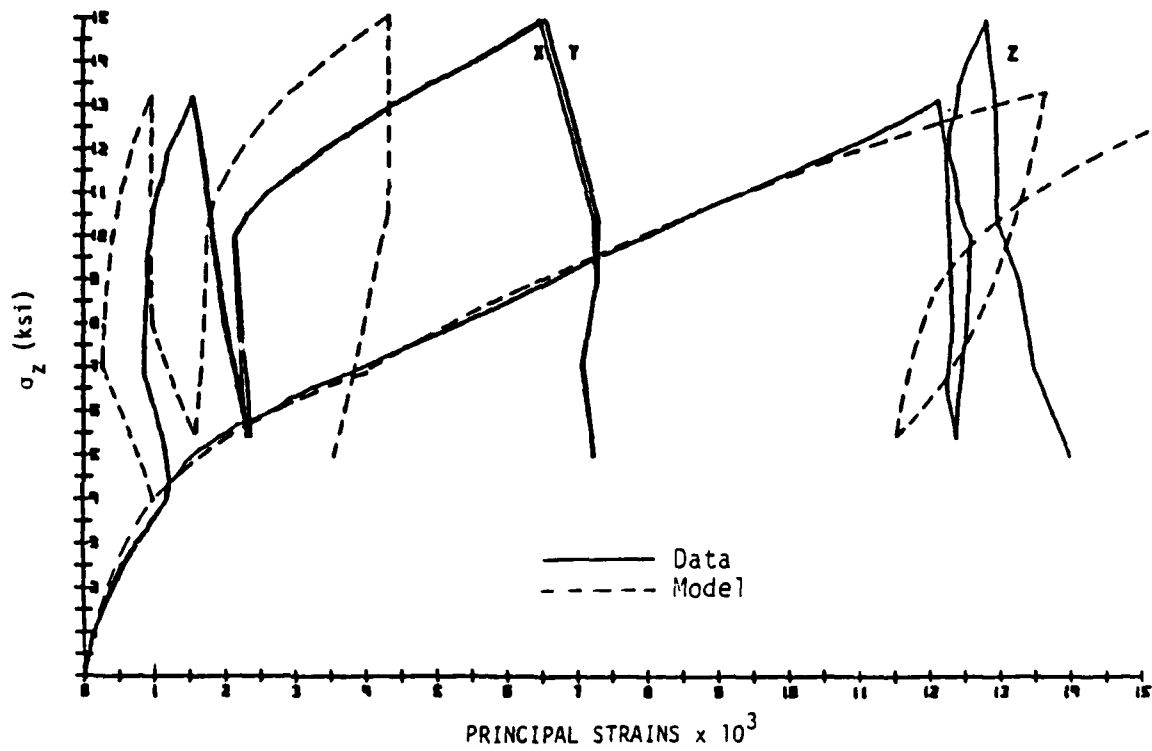


(b) Octahedral normal stress versus octahedral normal strain.

Figure 32. Measured and predicted responses for Test 4-17.



(a) Stress path.



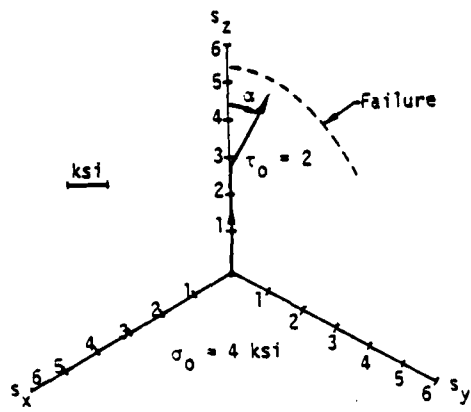
(b) Major principal stress versus principal strains.

Figure 33. Measured and predicted responses for Test 4-20.

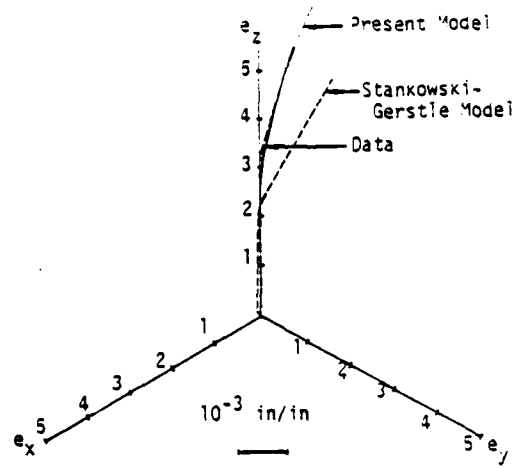
The final axisymmetric test to be considered here is Test 4-20. The prescribed stress path for this test consisted of nonproportional stress deviation, and is shown in Figure 33. The predicted response to this prescribed stress path, as well as the corresponding data, are also shown in Figure 33. Although some discrepancy between the model and the data is evident in the late stages of the stress history, the agreement during most of the stress history is excellent. Therefore, the overall agreement is considered good, considering the usual degree of scatter in concrete data; this test was also not repeated experimentally.

#### 5.4 SERIES NO. 5.

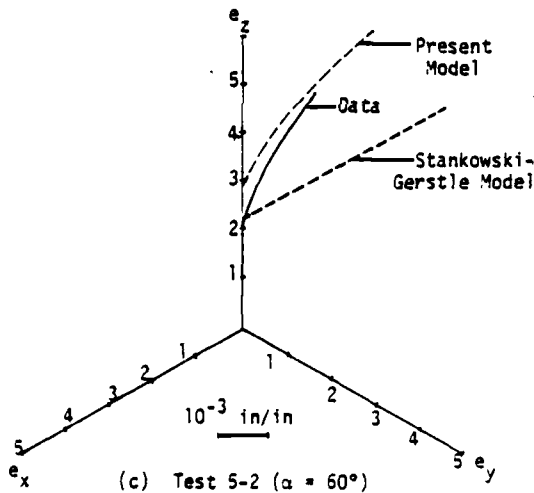
The purpose of the Series 5 tests was to investigate the response of plain concrete to unsymmetric stress paths in a given deviatoric plane. In the present study, attention was focussed on Tests 5-1 to 5-3 from this series, with emphasis on the behavior during the stress excursions in the deviatoric plane corresponding to  $\sigma_0 = 4$  ksi. Details of the prescribed stress paths for these tests are depicted in Figure 34(a). The measured and predicted deviatoric strain paths, corresponding to those portions of the stress paths in the deviatoric plane for Tests 5-1 to 5-3, are shown in Figure 34. Also included in this figure for comparative purposes are corresponding predictions made by Stankowski,<sup>(30)</sup> using the Stankowski-Gerstle model.<sup>(18)</sup> From an inspection of this figure, one observes that the point on the  $e_2$  axis at which the nonproportional portion of the path begins for the present model is consistently higher in all three tests than the data. It appears, therefore, that the model is too soft for proportional excursions from the hydrostatic axis out along the triaxial compression axis, confirming the same observation made earlier in conjunction with the circular stress paths in Series 3. Despite these small differences, however, Figure 34 shows that the present model does an excellent job of predicting the



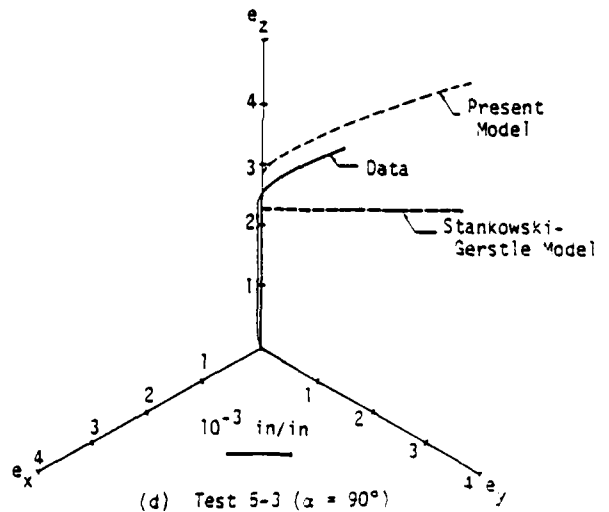
(a) Stress path.



(b) Test 5-1 ( $\alpha = 30^\circ$ )



(c) Test 5-2 ( $\alpha = 60^\circ$ )



(d) Test 5-3 ( $\alpha = 90^\circ$ )

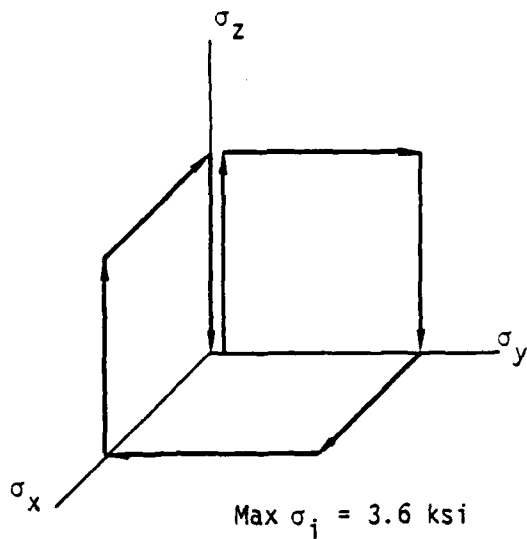
Figure 34. Stress paths for Tests 5-1 to 5-3.

measured responses in the deviatoric plane, and is clearly superior to the Stankowski-Gerstle model. (18)

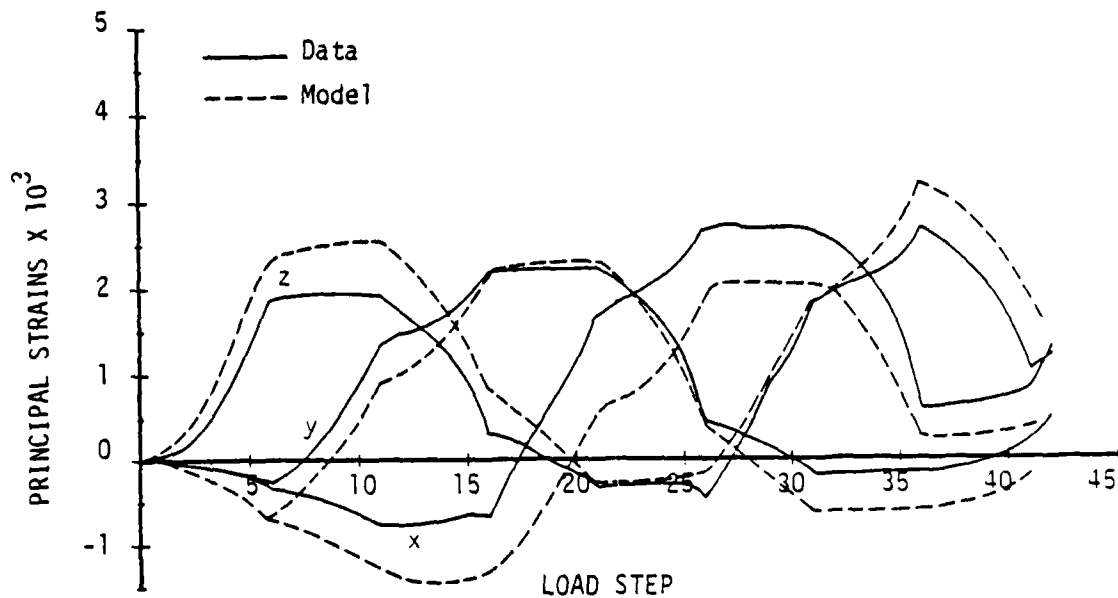
#### 5.5 SERIES NO. 6.

The tests in this series were designed to investigate the response of plain concrete to piecewise uniaxial load steps which formed closed loops. The loading was applied in a manner such that all possible uniaxial and equi-biaxial stress states of a given level were reached. Attention in the present study was focussed on Test 6-2, for which the prescribed stress history was as shown in Figure 35(a). The peak values of the principal stresses for this path were 3.6 ksi.

The response predicted by the present model to the prescribed stress path is illustrated in Figure 35(b), where the corresponding data are also given. Considering the typical scatter in concrete data, the agreement between the model prediction and the data is again considered excellent.



(a) Stress path



(b) Principal strains versus load step.

Figure 35. Measured and predicted responses for Test 6-2.

## SECTION 6

### CONCLUSIONS

An advanced nonlinear constitutive model has been developed, on the basis of the new endochronic plasticity theory, to describe the general behavior of plain concrete over the range of stresses where significant cracking does not occur. The model is isotropic, rate-independent and thermodynamically sound. It satisfies Drucker's Stability Postulate, Prager's Continuity Condition and the Second Law. The model exhibits shear-volumetric coupling in the form of shear compaction, dependence of shear behavior on hydrostatic pressure, hysteresis and stress-path dependence. The wide variety of proof-tests to which the model was subjected clearly demonstrate that, over the intended range of application, the present endochronic model provides an excellent description of the behavior of plain concrete.

Our future research activities will be devoted to extending the capabilities of the present model to a wider range of behavior; this will include focus on the following tasks:

- Modify the unloading-reloading shear behavior through the addition of shear hardening to more closely portray experimental data.
- Extend model to cover the range of behavior over which significant cracking occurs.
- Introduce strain-rate dependence.

- Develop an optimal (computationally efficient) numerical scheme for treating the model in large finite element computer codes.

To meet these goals, appropriate and quality experimental data will be required, which may necessitate additional advancements in testing methods (35)

## SECTION 7

### LIST OF REFERENCES

1. Chen, W. F., and H. Suzuki (1980), "Constitutive Models for Concrete," *Computers and Structures*, 12, 23.
2. Cedolin, L., Y. R. J. Crutzen and S. Dei Poli (1977), "Triaxial Stress-Strain Relationship for Concrete," *J. Engng. Mech. Div. ASCE*, 103, (EM3), 423.
3. Chen, A. C. T. and W. F. Chen (1975), "Constitutive Relations for Concrete," *J. Engng. Mech. Div. ASCE*, 101, (EM4), 465.
4. Coon, M. D., and R. J. Evans (1972), "Incremental Constitutive Laws and Their Associated Failure Criteria with Application to Plain Concrete," *Int. J. Solids Structs.*, 8, 1169.
5. Bazant, Z. P., and P. D. Bhat (1976), "Endochronic Theory of Inelasticity and Failure of Concrete," *J. Engng. Mech. Div. ASCE*, 102, (EM4), 701.
6. Bazant, Z. P., and C. L. Shieh (1978), "Endochronic Model for Non-linear Triaxial Behavior of Concrete," *Nuclear Engng. Design*, 47, 305.
7. Fardis, N. M., B. Alibe and J. L. Tassoulas (1983), "Monotonic and Cyclic Constitutive Law for Concrete," *J. Engng. Mech. Div. ASCE*, 109(2), 516.
8. Yang, B-L., Y. F. Dafalias and L. R. Herrmann (1983), "A Bounding Surface Plasticity Model for Concrete," presented at the ASCE Annual Convention, October 1983, Houston Session 53 on Development in Analytical and Theoretical Aspects of Constitutive Modeling.
9. Krajcinovic, D., and S. Selvaraj (1983), "Constitutive Equations for Concrete," in *Proc. Int. Confr. on Constitutive Laws for Engng. Matls.*, Tucson, Arizona.
10. Suaris, W., and S. P. Shah (1983), "A Strain-Rate Dependent Damage Model for Concrete," presented at the ASCE-EMD Specialty Conference, Purdue University.
11. Bazant, Z. P., and S. S. Kim (1979), "Plastic-Fracturing Theory for Concrete," *J. Engng. Mech. Div. ASCE*, 105, (EM3), 407.
12. Buyukozturk, O., A. H. Nilson and F. O. Slate (1972), "Deformation and Fracture of a Particulate Composite," *J. Engng. Mech. Div. ASCE*, 98, (EM3), 501.

AD-A172 512

AN ENDOCHRONIC PLASTICITY THEORY FOR CONCRETE(U)  
S-CUBED LA JOLLA CA K C VALANIS ET AL. 20 FEB 85  
SSS-R-85-7172 DNA-TR-85-158 DNA001-84-C-0127

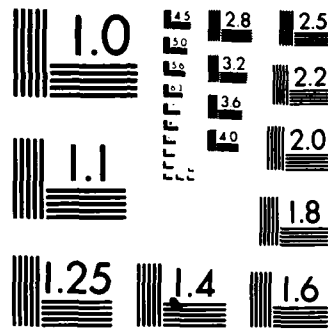
2/2

UNCLASSIFIED

F/G 20/11

ML





MICROCOPY RESOLUTION TEST CHART  
NATIONAL BUREAU OF STANDARDS-1963-A

13. Chen, W. F., and E. C. Ting (1980), "Constitutive Models for Concrete Structures," *J. Engng. Mech. Div. ASCE*, 106, (EM1), 1.
14. Mills, L. L., and R. M. Zimmerman (1970), "Compressive Strength of Plain Concrete Under Multiaxial Loading Conditions," *J. Amer. Concrete Inst.*, 67, (10), 802.
15. Launay, P., and H. Gachon (1970), "Strain and Ultimate Strength of Concrete Under Triaxial Stress," Special Publication SP-34, *Amer. Concrete Inst.*, Vol. 1, 269.
16. Linse, D. (1973), "Versuchsanlage zur Ermittlung der Dreiachsigen Festigkeit von Beton mit Erstern Versuchsergebnissen," *Cement and Concrete Research*, 3, (4), 445.
17. Scavuzzo, R., T. Stankowski, K. H. Gerstle and H. Y. Ko (1983), "Stress-Strain Curves for Concrete Under Multiaxial Load Histories," CEAE Department, Univ. of Colo., Boulder.
18. Stankowski, T., and K. H. Gerstle (1983), "Simple Formulation of Concrete Behavior Under Load Histories," submitted to *J. Amer. Concrete Inst.* for publication.
19. Gerstle, K. H. (1983), "Simple Formulation of Triaxial Concrete Behavior," *J. Amer. Concrete Inst.*, 78(5), 382.
20. Hsieh, S. S., E. C. Ting and W. F. Chen (1982), "A Plastic Fracture Model for Concrete," *Int. J. Solids Structs.*, 18(3), 181.
21. Valanis, K. C. (1979), "Endochronic Theory with Proper Hysteresis Loop Closure Properties," S-CUBED, La Jolla, California, Report No. SSS-R-80-4102.
22. Valanis, K. C., and C. F. Lee (1982), "Some Recent Developments of the Endochronic Theory with Applications," *Nuc. Eng. and Design*, 69, 327.
23. Valanis, K. C., and J. Fan (1983), "Endochronic Analysis of Cyclic Elastoplastic Strain Fields in a Notched Plate," *J. Appl. Mech.*, 50, 789.
24. Valanis, K. C., and H. E. Read (1982), "A new Endochronic Plasticity Model for Soils," in *SOIL MECHANICS-TRANSIENT AND CYCLIC LOADS*, G. H. Pande and D. C. Zienkiewicz, eds., John Wiley and Sons, Ltd.
25. Trangenstein, J. A., and H. E. Read (1982), "The Inelastic Response Characteristics of the New Endochronic Theory with Singular Kernel," *Int. J. Solids Struct.*, 18(11), 947.

26. Murakami, H., and H. E. Read (1984), "Endochronic Plasticity: Some basic properties of Plastic Flow," presented at the 21st Annual Meeting of the Society of Engineering Science, VPI, Blacksburg, VA October 15-17. See, also, *Int. J. Solids Struct.*, 22, (1986).
27. Bazant, Z. P., and C.-L. Shieh (1980), "Hysteretic Fracturing Endochronic Theory for Concrete," *J. Engng. Mech. Div. ASCE*, 106, (EM5), 929.
28. Valanis, K. C. (1971), "A Theory of Viscoplasticity Without a Yield Surface, Part I: General Theory," *Arch. of Mechs*, 23, 517.
29. Bazant, Z. P., R. J. Krizek and C.-L. Shieh (1985), Closure to the paper "Hysteretic Endochronic Theory for Sand," *J. Engng. Mechs. Div. ASCE*, 111(1), 103.
30. Stankowski, T. (1983), "Concrete Under Multiaxial Load Histories," M. S. Thesis, CEAE Department, University of Colorado, Boulder.
31. Valanis, K. C., and C. F. Lee (1983), "Endochronic Plasticity, Physical Basis and Applications," *Proc. Intl. Conf. on Constitutive Laws for Engng. Matls., Theory and Appls.*, Edited by C. S. Desai, Tucson, Arizona.
32. Valanis, K. C., and C. F. Lee (1982), "Deformation Kinetic Theory of Creep in Metals," *Res. Mechanica*, 5, 159.
33. Gerstle, K. H., and K. Willam (1982), Presentation at ASCE Conference on Material Modeling, New Orleans, Louisiana, April.
34. Read, H. E., (1985), Discussion of the paper "Hysteretic Endochronic Theory for Sand," by Z. P. Bazant, R. J. Krizek and C.-L. Shieh, *J. Engr. Mechs*, 111(1), 103.
35. Hegemier, G. A., and H. E. Read (1985), "On Flow and Deformation of Brittle Solids: Some Outstanding Issues," *Mechanics of Materials*, 4, 215.

APPENDIX A

A PROOF OF EQUATION (3.50)

The purpose of this appendix is to show that

$$\lim_{z \rightarrow \infty} \int_0^z \rho(z - z') \left( \frac{cz'}{1 + cz'} \right)^{1/2} dz' = M_{\infty} \quad (\text{A.1})$$

where

$$c > 0, M(z) = \int_0^z \rho(z') dz' \quad (\text{A.2a, b})$$

and

$$M_{\infty} = M(\infty) < \infty \quad (\text{A.3})$$

Here,  $\rho(z)$  is a positive monotonically decreasing function of  $z$  in the domain  $0 < z < \infty$  and

$$\lim_{z \rightarrow \infty} \rho(z) = 0 \quad (\text{A.4a})$$

Therefore,  $M(z)$  is positive, monotonically increasing and convex in the sense that

$$M(z) - M(z - a) < a \left. \frac{dM}{dz} \right|_{z-a} \quad (\text{A.4b})$$

Thus in view of Eqs. (A.2b) and (A.4)

$$M(z) - M(z - a) < a\rho(z - a) \quad (\text{A.4c})$$

It follows from Eqs. (A.4a) and (A.4c) that

$$\lim_{z \rightarrow \infty} \{M(z) - M(z - a)\} = 0 \quad (\text{A.5})$$

To prove the validity of Eq. (A.1) we first prove the following theorem.

Theorem: Let  $R(z)$  be a positive monotonically decreasing function bounded from above and below in the sense that

$$0 < R(z) \leq R(0) \quad (\text{A.6})$$

and

$$\lim_{z \rightarrow \infty} R(z) = 0 \quad (\text{A.7})$$

The operational definition of Eq. (A.7) is the following: Given an  $\epsilon$  however small there exists a  $z < \infty$  such that

$$R(z) < \epsilon \quad (\text{A.8a})$$

Then the following is true:

$$\lim_{z \rightarrow \infty} \int_0^z \rho(z - z')R(z')dz' = 0 \quad (\text{A.8b})$$

Proof:

The integral I on the lefthand side of Eq. (A.8b) may be written in the form

$$I = \int_0^{z_0} \rho(z - z')R(z')dz' + \int_{z_0}^z \rho(z - z')R(z')dz' \quad (\text{A.9})$$

where  $0 < z_0 < z$ . Because of the properties of  $R(z)$ , it follows that

$$\int_0^{z_0} \rho(z - z')R(z')dz' < R(0) \int_0^{z_0} \rho(z - z')dz' \quad (\text{A.10})$$

Or, in view of Eq. (A.2b),

$$\int_0^{z_0} \rho(z - z')R(z')dz' < R(0) \{M(z) - M(z - z_0)\} \quad (\text{A.11})$$

Hence, as a result of Eq. (A.5)

$$\lim_{z \rightarrow \infty} \int_0^{z_0} \rho(z - z')R(z')dz' = 0 \quad (\text{A.12})$$

Also, following the same reasoning as above,

$$\int_{z_0}^z \rho(z - z')R(z')dz' < R(z_0)M(z - z_0) \quad (\text{A.13})$$

Hence:

$$\lim_{z \rightarrow \infty} \int_{z_0}^z \rho(z - z') R(z') dz' < M_{\infty} R(z_0) \quad (\text{A.14})$$

Now because of the properties of  $R(z)$ , i.e., Eqs. (A.8a) and (A.8b), the righthand side of Eq. (A.14) can be made as small as one pleases, in the sense that given an  $\epsilon$  however small there exists a  $z_0$  such that

$$M R(z_0) < \epsilon \quad (\text{A.15})$$

Since  $z_0$  may be any large finite number,  $M_{\infty} R(z_0)$  may differ from zero by an amount which can be made as small as one pleases. In view, therefore, of Eqs. (A.12) and (A.15), Eq. (A.8) is true and the theorem is proved.

Returning to Eq. (A.1), we note that proving this equation is tantamount to showing that

$$\lim_{z \rightarrow \infty} \int_0^z \rho(z - z') \left\{ 1 - \frac{cz'}{1 + cz'} \right\}^{1/2} dz' = 0 \quad (\text{A.16})$$

Hence, since the function  $1 - cz'/(1 + cz')$  has the properties of  $R(z)$ , Eq. (A.16) and hence Eq. (A.1) are proved.

## APPENDIX B

### NUMERICAL SCHEME FOR TREATING THE PRESENT CONSTITUTIVE MODEL UNDER STRESS-DRIVEN CONDITIONS

The numerical scheme used to generate the model predictions presented in this report is described below. The approach consists of an explicit incremental Euler scheme developed specifically for numerically treating the governing system of equations for the model under stress-driven conditions. Due to its explicit nature, care must be taken to insure that the prescribed increments are sufficiently small that the computed behavior is independent of the increment size. Otherwise, the scheme is straightforward, efficient and easy to implement.\*

The basic system of equations which govern the behavior of the model are as follows:

$$\xi = \int_0^{z_s} \rho(z_s - z') \frac{d\epsilon^p}{dz'} dz' \quad (\text{B.1})$$

$$\sigma = \int_0^{z_H} \phi(z_H - z') \frac{d\epsilon^p}{dz'} dz' \quad (\text{B.2})$$

$$d\xi = 2\mu(d\epsilon - d\epsilon^p) \quad (\text{B.3})$$

---

\*. This numerical scheme is due to Dr. H. Murakami, a consultant to S-CUBED and Assistant Professor, University of California, San Diego.

$$d\sigma = K(d\epsilon - d\epsilon^P) \quad (\text{B.4})$$

$$dz^2 = \left| \left| d\epsilon^P \right| \right|^2 + k^2(d\epsilon^P)^2 \quad (\text{B.5})$$

$$dz_s = dz/F_s \quad (\text{B.6})$$

$$dz_H = dz/(kF_H) \quad (\text{B.7})$$

Following the approach described in Section 2, the kernel functions  $\rho(z_s)$  and  $\phi(z_H)$  are represented by exponential series of the form:

$$\rho = \sum_r A_r e^{-a_r z_s} \quad (\text{B.8})$$

$$\phi = \sum_i B_i e^{-\beta_i z_H} \quad (\text{B.9})$$

It then follows that the expressions for  $\xi$  and  $\sigma$  given by Eqs. (B.1) and (B.2) can be alternately written as

$$\xi = \sum_r Q_r \quad (\text{B.10})$$

$$\sigma = \sum_i P_i \quad (\text{B.11})$$

where  $Q_r$  and  $P_i$  satisfy the following ordinary differential equations:

$$\frac{dQ_r}{dz_s} + a_r Q_r = A_r \frac{de^P}{dz_s} \quad (\text{B.12})$$

$$\frac{dP_i}{dz_H} + \beta_i P_i = B_i \frac{de^P}{dz_H} \quad (\text{B.13})$$

From Eqs. (B.10) to (B.13), we can write:

$$dz_s = \bar{A} de^P - Q dz_s \quad (\text{B.14})$$

$$d\sigma = \bar{B} de^P - P dz_H \quad (\text{B.15})$$

where

$$\bar{A} = \sum_r A_r$$

$$Q = \sum_r a_r Q_r \quad (\text{B.16})$$

$$\bar{B} = \sum_i B_i$$

$$P = \sum_i \beta_i P_i$$

Introducing Eqs. (B.6) and (B.7) into Eqs. (B.14) and (B.15) leads to the expressions:

$$de^P = \frac{1}{\bar{A}} \left( dz_s + \frac{Q}{\bar{A}} dz \right) \quad (\text{B.17})$$

$$d\epsilon^P = \frac{1}{B} \left( d\sigma + \frac{P}{kF_H} dz \right) \quad (B.18)$$

which when combined with Eq. (B.5), leads to the following quadratic expression for dz:

$$a dz^2 + b dz + c = 0 \quad (B.19)$$

where

$$\left. \begin{aligned} a &= 1 - \frac{Q \cdot Q}{(\bar{A} F_s)^2} - \left( \frac{P}{B F_H} \right)^2 \\ b &= -2 \left( \frac{Q \cdot d\bar{s}}{\bar{A}^2 F_s} + \frac{kP}{B^2 F_H} d\sigma \right) \\ c &= - \left[ \frac{d\bar{s} \cdot d\bar{s}}{\bar{A}^2} + \left( \frac{k d\sigma}{B} \right)^2 \right] \end{aligned} \right\} \quad (B.20)$$

Thus, for prescribed values of  $d\bar{s}$  and  $d\sigma$ , dz is given by the equation:

$$dz = - \frac{b}{2a} + \frac{1}{2a} \sqrt{b^2 - 4ac} \quad (B.12)$$

and by using Eqs. (B.17) and (B.18),  $d\epsilon^P$  and  $d\epsilon$  can then be found, after which  $d\bar{e}$  and  $d\epsilon$  are determined from Eqs. (B.3) and (B.4). Therefore, this approach allows the strain increments  $d\bar{e}$  to be found for prescribed increments in the stress  $d\bar{g}$ .

## APPENDIX C

### DERIVATION OF EQUATION (4.12)

When  $\sigma$  is on the linear portion of the hydrostatic stress-strain curve, it follows, from Eq. (3.37), that

$$\sigma = k K_o (1 + \beta S_H) \frac{dS_H}{dz} \quad (C.1)$$

This expression may be combined with Eq. (3.36), i.e.,

$$dz^2 = dS_s^2 + k^2 dS_H^2 \quad (C.2)$$

to give the following result:

$$dz \left\{ 1 - \left[ \frac{\sigma_1}{K_o(1 + \beta S)} \right]^2 \right\}^{1/2} = dS_s \quad (C.3)$$

where  $\sigma_1$  denotes the reference pressure on the linear portion of the hydrostat.

We may decompose  $S_H$  into two terms and write:

$$K_o(1 + \beta S_H) = K_o(1 + \beta S_H^c) + K_o \beta S_H^s \quad (C.4)$$

where  $S_H^c$  is the value of  $S_H$  due solely to hydrostatic compression, while  $S_H^s$  is the component due strictly to shear. For shear at  $\sigma = \sigma_1$ , it follows that

$$\sigma_1 = K_o(1 + \beta S_H) \quad (C.4)$$

Hence, Eq. (C.4) can be rewritten in the form:

$$K_o(1 + \beta S_H) = \sigma_1 + K_o \beta S_H^s \quad (C.5)$$

Upon substituting Eq. (C.5) into Eq. (C.3), we obtain the result

$$\frac{dS_s}{dz} = \left\{ 1 - \left[ \frac{1}{1 + \frac{K_o \beta}{\sigma_1} S_H^s} \right]^2 \right\}^{1/2} \quad (C.6)$$

When  $\sigma = \sigma_1$ , it follows from Eq. (C.1) that

$$\sigma_1 = k K_o \left( 1 + \beta S_H + \beta S_H^s \right) \frac{d S_H^s}{dz} \quad (C.7)$$

so that

$$dz = k \left( 1 + \frac{K_o \beta}{\sigma_1} S_H^s \right) d S_H^s \quad (C.8)$$

Let

$$y = z = z' \quad (C.9)$$

$$x = 1 + \frac{K_o \beta}{\sigma_1} S_H^s \quad (C.10)$$

where  $z'$  denotes the value of  $z$  at which shearing begins. Then Eq. (C.8) can be written

$$dy = \left( \frac{k\sigma_1}{K_o\beta} \right) x \, dx \quad (C.11)$$

Integrating yields

$$y = \frac{1}{2a} (x^2 - 1) \quad (C.12)$$

where we have set

$$a = \frac{\beta K_o}{k\sigma_1} \quad (C.13)$$

From Eqs. (C.6) and (C.10), it follows that

$$\frac{d\zeta_s}{dz} = \left[ 1 - \left( \frac{1}{x} \right)^2 \right]^{1/2} \quad (C.14)$$

Using Eq. (C.13), we can rewrite Eq. (3.11) in the form:

$$dz = \frac{x \, dx}{a} \quad (C.15)$$

since  $dy = dz$ . Eqs. (C.14) and (C.15) may now be combined to give

$$d\zeta_s = \frac{1}{a} (x^2 - 1)^{1/2} \, dx \quad (C.16)$$

which, upon integration, leads to the result:

$$\zeta_s = \frac{1}{2a} \left\{ x \sqrt{x^2 - 1} - \log \left| x + \sqrt{x^2 - 1} \right| \right\} \quad (C.17)$$

But from (C.12), we have

$$\begin{aligned}x^2 - 1 &= 2 ay \\x^2 &= 1 + 2 ay\end{aligned}\tag{C.18}$$

which, in view of Eq. (C.9), may be rewritten in the form:

$$\begin{aligned}x^2 - 1 &= 2a z_s \\x^2 &= 1 + 2a z_s\end{aligned}\tag{C.19}$$

since for  $F_s = 1$ , we have

$$dz_s = dz$$

and

$$z_s = z - z' \tag{C.20}$$

Upon combining Eqs. (C.17) and (C.19), the following expression is obtained:

$$S_s = \frac{1}{2a} \left\{ \sqrt{2a z_s} \sqrt{1 + 2a z_s} - \log \left| \sqrt{2a z_s} + \sqrt{1 + 2a z_s} \right| \right\} \tag{C.21}$$

which is Eq. (4.12) given in the main text.

## DISTRIBUTION LIST

### DEPARTMENT OF DEFENSE

ASST TO THE SECY OF DEFENSE ATOMIC ENERGY  
ATTN: EXECUTIVE ASSISTANT

DEFENSE INTELLIGENCE AGENCY  
ATTN: DB-4D  
ATTN: DT-2  
ATTN: RTS-2B

DEFENSE NUCLEAR AGENCY  
ATTN: SPAS  
ATTN: SPSS  
ATTN: SPTD  
ATTN: STSP  
4 CYS ATTN: STTI-CA

DEFENSE TECHNICAL INFORMATION CENTER  
12 CYS ATTN: DD

FIELD COMMAND DNA DET 2  
LAWRENCE LIVERMORE NATIONAL LAB  
ATTN: FC-1

FIELD COMMAND DEFENSE NUCLEAR AGENCY  
ATTN: FCTT W SUMMA  
ATTN: FCTXE

JOINT CHIEFS OF STAFF  
ATTN: G750 J-5 FORCE PLNG & PROG DIV  
ATTN: J-5 NUC & CHEM DIV  
ATTN: JAD/SFD  
ATTN: JAD/SSD

UNDER SECY OF DEF FOR RSCH & ENGRG  
ATTN: STRAT & SPACE SYS (OS)  
ATTN: STRAT & THEATER NUC FOR F VAJDA

### DEPARTMENT OF THE ARMY

DEP CH OF STAFF FOR OPS & PLANS  
ATTN: DAMO-NCZ

HARRY DIAMOND LABORATORIES  
ATTN: SLCHD-NW-P J GWALTNEY 20240

U S ARMY BALLISTIC RESEARCH LAB  
ATTN: SLCBR-SS-T TECH LIB

U S ARMY MATERIAL TECHNOLOGY LABORATORY  
ATTN: DRXMR-HH J DIGNAM

U S ARMY NUCLEAR & CHEMICAL AGENCY  
ATTN: LIBRARY

U S ARMY TRADOC SYS ANALYSIS ACTVY  
ATTN: ATAA-TDC R BENSON

US ARMY MISSILE COMMAND  
ATTN: AMSMI-RD-DEP W THOMAS  
ATTN: AMSMI-RD-UB H GREENE

### DEPARTMENT OF THE NAVY

NAVAL RESEARCH LABORATORY  
ATTN: CODE 2627 TECH LIB  
ATTN: CODE 4650 A WILLIAMS  
ATTN: CODE 4770 G COOPERSTEIN

NAVAL SEA SYSTEMS COMMAND  
ATTN: SEA-0352 M KINNA

NAVAL WEAPONS EVALUATION FACILITY  
ATTN: CLASSIFIED LIBRARY

OFC OF THE DEPUTY CHIEF OF NAVAL OPS  
ATTN: NOP 654 STRAT EVAL & ANAL BR

STRATEGIC SYSTEMS PROGRAMS(PM-1)  
ATTN: SP-272

### DEPARTMENT OF THE AIR FORCE

AERONAUTICAL SYSTEMS DIVISION, AFSC  
ATTN: ASD/ENSSS H GRIFFIS

AIR FORCE ROCKET PROPULSION LAB  
ATTN: LKCS G BEALE

AIR FORCE SYSTEMS COMMAND  
ATTN: SDM  
ATTN: XRTO

AIR FORCE WEAPONS LABORATORY, AFSC  
ATTN: HO R DUFFNER  
ATTN: NTA A SHARP  
ATTN: NTES  
ATTN: SUL

AIR FORCE WRIGHT AERONAUTICAL LAB  
ATTN: FIMG

AIR FORCE WRIGHT AERONAUTICAL LAB  
ATTN: AFWAY MLBT W ANSPACH

AIR UNIVERSITY LIBRARY  
ATTN: AUL-LSE

**DEPARTMENT OF THE AIR FORCE (CONTINUED)**

**BALLISTIC MISSILE OFFICE/DAA**

ATTN: ENSN  
ATTN: ENSR  
ATTN: MYE

**DEPUTY CHIEF OF STAFF/AF-RDQI**

ATTN: AF/RDQI

**HEADQUARTERS U S AIR FORCE**

ATTN: AFXOOTS

**DEPARTMENT OF ENERGY**

**DEPARTMENT OF ENERGY**

ATTN: OMA/DP-225

**UNIVERSITY OF CALIFORNIA  
LAWRENCE LIVERMORE NATIONAL LAB**

ATTN: L-125 J KELLER  
ATTN: L-262 J KNOX  
ATTN: L-8 P CHRZANOWSKI

**LOS ALAMOS NATIONAL LABORATORY**

ATTN: E548 R S DINGUS  
ATTN: MS670 T T SCOLMAN  
ATTN: R S THURSTON  
ATTN: R W SELDEN

**SANDIA NATIONAL LABORATORIES**

ATTN: EDUC AND TECH LIB DIV  
ATTN: H NORRIS

**SANDIA NATIONAL LABORATORIES**

ATTN: M B COWAN  
ATTN: ORG 7112 A CHABAI

**OTHER GOVERNMENT**

**CENTRAL INTELLIGENCE AGENCY**

ATTN: OSWR/NED

**DEPARTMENT OF DEFENSE CONTRACTORS**

**ACUREX CORP**

ATTN: C NARDO

**AEROJET GENERAL CORP**

ATTN: A COLLINS

**AEROSPACE CORP**

ATTN: M2-250

**ANALYTIC SERVICES, INC (ANSER)**

ATTN: J SELIG

**APTEK, INC**

ATTN: T MEAGHER

**BOEING CO**

ATTN: R L DYRDHAL

ATTN: A DACOSTA

ATTN: E YORK

**BOEING MILITARY AIRPLANE CO**

ATTN: D SAWDY

**CALIFORNIA RESEARCH & TECHNOLOGY, INC**

ATTN: K KREYENHAGEN

**CALSPAN CORP**

ATTN: M DUNN  
ATTN: M HOLDEN

**CARPENTER RESEARCH CORP**

ATTN: H J CARPENTER

**G B LABORATORY, INC**

ATTN: G BURGHART

**GENERAL ELECTRIC CO**

ATTN: A GARBER, RM 6418  
ATTN: B MAGUIRE

**HERCULES, INC**

ATTN: P MCALLISTER

**INSTITUTE FOR DEFENSE ANALYSES**

ATTN: CLASSIFIED LIBRARY

**KAMAN SCIENCES CORP**

ATTN: L MENTE  
ATTN: R RUETENIK  
ATTN: W LEE

**KAMAN SCIENCES CORP**

ATTN: F SHELTON  
ATTN: J HOFFMAN  
ATTN: J KEITH

**KAMAN TEMPO**

ATTN: DASIAC

**KAMAN TEMPO**

ATTN: DASIAC

**LOCKHEED MISSILES & SPACE CO, INC**

ATTN: F BORGARDT

**LOCKHEED MISSILES & SPACE CO, INC**

ATTN: R WALZ

**MARTIN MARIETTA DENVER AEROSPACE**

ATTN: E STRAUSS

**MCDONNELL DOUGLAS CORP**

ATTN: J KIRBY  
ATTN: J PECK  
ATTN: L COHEN

**MCDONNELL DOUGLAS CORP**

ATTN: M POTTER

**DEPT OF DEFENSE CONTRACTORS (CONTINUED)**

MORTON THIOKOL, INC  
ATTN: K HESS

PACIFIC-SIERRA RESEARCH CORP  
ATTN: H BRODE, CHAIRMAN SAGE

PHYSICS INTERNATIONAL CO  
ATTN: J SHEA

R & D ASSOCIATES  
ATTN: F A FIELD  
ATTN: P RAUSCH

RAND CORP  
ATTN: P DAVIS

RAND CORP  
ATTN: B BENNETT

S-CUBED  
ATTN: G GURTMAN  
2 CYS ATTN: H READ  
2 CYS ATTN: K VALANIS  
ATTN: R DUFF

SCIENCE APPLICATIONS INTL CORP  
ATTN: J WARNER  
ATTN: W PLOWS  
ATTN: W YENGST

SCIENCE APPLICATIONS INTL CORP  
ATTN: J COCKAYNE  
ATTN: W LAYSON

SCIENCE APPLICATIONS INTL CORP  
ATTN: A MARTELLUCCI

SCIENCE APPLICATIONS INTL CORP  
ATTN: J MANSHIP

SOUTHERN RESEARCH INSTITUTE  
ATTN: C PEARS

SRI INTERNATIONAL  
ATTN: D CURRAN

TECHNOLOGY DEVELOPMENT ASSOCIATES  
ATTN: N DISPENSIERE

TOYON RESEARCH CORP  
ATTN: B GRAGG  
ATTN: J CUNNINGHAM

TRW ELECTRONICS & DEFENSE SECTOR  
ATTN: A ZIMMERMAN  
ATTN: D BAER  
ATTN: M SEIZEW  
ATTN: N LIPNER  
ATTN: P BRANDT  
ATTN: R BACHARACH  
ATTN: R PLEBUCH HARD & SURV LAB  
ATTN: W WOOD

TRW ELECTRONICS & DEFENSE SECTOR  
ATTN: D KENNEDY  
ATTN: E ALLEN  
ATTN: E WONG  
ATTN: L BERGER  
ATTN: N GUILLES  
ATTN: P DAI  
ATTN: V BLANKINSHIP  
ATTN: W POLICH

END

10-86

DTIC